



NRL/MR/6790--07-9032

Propagation of High Energy Laser Beams in Various Environments

PHILLIP SPRANGLE

JOSEPH PEÑANO

*Beam Physics Branch
Plasma Physics Division*

BAHMAN HAFTZI

*Icarus Research, Inc.
Bethesda, Maryland*

June 8, 2007

20070912342

REPORT DOCUMENTATION PAGE				Form Approved OMB No. 0704-0188	
Public reporting burden for this collection of information is estimated to average 1 hour per response, including the time for reviewing instructions, searching existing data sources, gathering and maintaining the data needed, and completing and reviewing this collection of information. Send comments regarding this burden estimate or any other aspect of this collection of information, including suggestions for reducing this burden to Department of Defense, Washington Headquarters Services, Directorate for Information Operations and Reports (0704-0188), 1215 Jefferson Davis Highway, Suite 1204, Arlington, VA 22202-4302. Respondents should be aware that notwithstanding any other provision of law, no person shall be subject to any penalty for failing to comply with a collection of information if it does not display a currently valid OMB control number. PLEASE DO NOT RETURN YOUR FORM TO THE ABOVE ADDRESS.					
1. REPORT DATE (DD-MM-YYYY) 08-06-2007		2. REPORT TYPE Final		3. DATES COVERED (From - To) May 2004 – May 2006	
4. TITLE AND SUBTITLE Propagation of High Energy Laser Beams in Various Environments				5a. CONTRACT NUMBER	
				5b. GRANT NUMBER	
				5c. PROGRAM ELEMENT NUMBER	
6. AUTHOR(S) Phillip Sprangle, Joseph Peñano, and Bahman Hafizi*				5d. PROJECT NUMBER 67-8352-A7	
				5e. TASK NUMBER	
				5f. WORK UNIT NUMBER	
7. PERFORMING ORGANIZATION NAME(S) AND ADDRESS(ES) Naval Research Laboratory, Code 6790 4555 Overlook Avenue, SW Washington, DC 20375-5320				8. PERFORMING ORGANIZATION REPORT NUMBER NRL/MR/6790--07-9032	
9. SPONSORING / MONITORING AGENCY NAME(S) AND ADDRESS(ES) Office of Naval Research One Liberty Center 875 North Randolph St. Arlington, VA 22203-1995				10. SPONSOR / MONITOR'S ACRONYM(S) ONR	
				11. SPONSOR / MONITOR'S REPORT NUMBER(S)	
12. DISTRIBUTION / AVAILABILITY STATEMENT Approved for public release; distribution is unlimited.					
13. SUPPLEMENTARY NOTES *Icarus Research, Inc., P.O. Box 30780, Bethesda, MD 20874-0780					
14. ABSTRACT We report the results of our theoretical study on the key physical processes that affect the propagation of high energy lasers in the atmosphere. The main objective of this study is to discuss the optimum laser wavelength and power for efficient propagation in maritime, desert, rural and urban atmospheric environments. The theoretical/numerical model used in this study includes the effects of aerosol and molecular scattering, aerosol heating and vaporization, thermal blooming due to aerosol and molecular absorption, atmospheric turbulence, and beam quality. These processes are modeled in a fully three-dimensional and time-dependent manner. It is found that aerosol particles are particularly important because they result in laser scattering, absorption and enhanced thermal blooming. In the water vapor transmission windows, the total absorption coefficient driving thermal blooming can be caused mainly by aerosols and not water vapor. In certain maritime environments the deleterious effects of aerosols can be reduced by vaporization. Aerosol particles which cannot be vaporized, such as those consisting of dust, soot, etc., can significantly increase thermal blooming. The optimum wavelength and power for propagation are found for each atmospheric environment.					
15. SUBJECT TERMS Propagation Laser beam Thermal blooming High energy lasers Aerosols					
16. SECURITY CLASSIFICATION OF:			17. LIMITATION OF ABSTRACT UL	18. NUMBER OF PAGES 60	19a. NAME OF RESPONSIBLE PERSON Phillip Sprangle
a. REPORT Unclassified	b. ABSTRACT Unclassified	c. THIS PAGE Unclassified			19b. TELEPHONE NUMBER (include area code) (202) 767-3493

Final Technical Report

**Propagation of High Energy Laser Beams in Various
Environments**

**Prepared for
HIGH-ENERGY-LASER JOINT TECHNOLOGY OFFICE**

For the period

May 2004 to May 2006

Prepared by

Phillip Sprangle (Principal Investigator)

Joseph Peñano

Bahman Hafizi*

* Icarus Research, Inc., P.O. Box 30780, Bethesda, MD 20824-0780

**Naval Research Laboratory
Plasma Physics Division
Washington, DC**

CONTENTS

SUMMARY.....	iv
I. INTRODUCTION	1
II. PHYSICAL PROCESSES AFFECTING HEL PROPAGATION.....	4
i) Beam quality	
ii) Turbulence	
iii) Molecular scattering	
iv) Aerosol scattering	
v) Aerosol thermal scattering	
vi) Thermal blooming due to water vapor absorption	
vii) Aerosol induced thermal blooming	
III. ATMOSPHERIC AEROSOLS	11
IV. AEROSOL HEATING AND VAPORIZATION	17
i) Vaporization of an aerosol droplet	
ii) Vaporization of a distribution of aerosols	
V. THERMAL BLOOMING IN THE PRESENCE OF AEROSOLS.....	22
VI. SIMULATIONS OF HEL PROPAGATION	25
i) Maritime Environment	
ii) Desert Environment	
iii) Rural Environment	
iv) Urban Environment	
v) Air-to-Ground (Desert and Urban Environments)	
VII. HEL PROPAGATION THROUGH STAGNATION ZONES.....	38
i) Analysis	
ii) Numerical Simulation	
iii) Results	
VIII. CONCLUSIONS	49
ACKNOWLEDGMENTS.....	52

SUMMARY

We report the results of our theoretical/computational study on the key physical processes that affect the propagation of high energy lasers in the atmosphere. The main objective of this study is to discuss the optimum laser wavelength and power for efficient propagation in maritime, desert, rural and urban atmospheric environments. The theoretical/numerical model used in this study includes the effects of aerosol and molecular scattering, aerosol heating and vaporization, thermal blooming due to aerosol and molecular absorption, atmospheric turbulence, and beam quality. These processes are modeled in a fully three-dimensional and time-dependent manner. It is found that aerosol particles, which consist of water, sea salt, organic matter, dust, soot, biomass smoke, urban pollutants, etc., are particularly important because they result in laser scattering, absorption and enhanced thermal blooming. In the water vapor transmission windows, the total absorption coefficient driving thermal blooming can be caused mainly by aerosols and not water vapor. In certain maritime environments the deleterious effects of aerosols can be reduced by vaporization. Aerosol particles which cannot be vaporized, such as those consisting of dust, soot, etc., can significantly increase thermal blooming. We show that moderate values of the laser beam quality parameter have little effect on the propagation efficiency. The laser power, averaged over dwell time, delivered to a distant target as a function of transmitted power is obtained for a number of wavelengths and atmospheric environments. The optimum wavelength and power are found for each atmospheric environment.

For the particular propagation geometry shown in Fig. 1, our results show that the average power on target is strongly dependent on the atmospheric environment:

Maritime: In a maritime environment, for transmitted power $P_T < 1.5$ MW, the propagation efficiency varies from $\eta \approx 50\%$ to 70% . In this transmitted power range the $1.625 \mu\text{m}$, and $2.141 \mu\text{m}$ wavelengths provide slightly greater efficiency than $1.045 \mu\text{m}$. However, for $P_T > 1.5$ MW, thermal blooming limits the power on target. In this high power regime, the optimum wavelength is $1.045 \mu\text{m}$ due to stronger absorption at the other wavelengths (see Fig. 5).

Desert: The aerosols in a desert environment are composed mainly of dust particles, however, the gross extinction coefficients are similar to that of a maritime environment. Hence, the power on target for the desert environment is very similar to the maritime environment for $P_T < 1.5$ MW (see Fig. 7). At higher transmitted powers, however, there is slightly less thermal blooming for $1.045 \mu\text{m}$ compared to the maritime environment due to the relatively lower aerosol absorption in a desert environment.

Rural: For the rural environment $2.141 \mu\text{m}$ is the optimum wavelength over the entire range of transmitted powers, $P_T < 3$ MW. The optimum power is found to be $P_T \sim 1.5$ MW which results in an average power on target of $\langle P_{\text{target}} \rangle \sim 0.6$ MW and efficiency of $\eta \approx 40\%$. For $P_T > 1.5$ MW, the power on target does not increase with transmitted power because of thermal blooming.

Urban: The optimum wavelength for the urban environment is found to be $2.141 \mu\text{m}$ over the entire range $P_T < 3$ MW (see Fig. 9). However, thermal blooming due to the non-hygroscopic aerosols places severe limits on the transmitted power. For example, the maximum value of $\langle P_{\text{target}} \rangle \sim 0.08$ MW is obtained for $P_T \sim 0.2$ MW, giving an efficiency of $\eta \approx 40\%$ (Fig.9).

Air to Ground (Desert, Urban): We have also considered vertical propagation scenarios from a fast moving platform to a stationary target on the ground in both a desert and urban environment. In these cases we find that for the desert environment, the large beam slew negates thermal blooming effects and results in high propagation efficiency, $\eta > 60\%$ for $2.141 \mu\text{m}$. In the urban environment, however, the presence of soot aerosols can still result in significant thermal blooming (see Fig. 10).

An approximate expression for the Strehl ratio of a focused HEL beam propagating through a stagnant zone is derived. The propagation of a HEL beam in a maritime atmosphere with a stagnation zone is modeled using the HELCAP code. The laser power delivered to the target is calculated as a function of slew rate. For the parameters considered, it is found that a stagnation zone near the laser source has little effect on the propagation efficiency while a stagnation zone near the target can significantly reduce the power on the target.

I. Introduction

High energy lasers (HELs) have a number of directed energy (DE) applications requiring high-intensity beams to be propagated long distances under a wide range of atmospheric conditions. The optimum wavelength for efficient HEL propagation depends on the atmospheric conditions and a number of inter-related physical processes which include: thermal blooming due to aerosol and molecular absorption [1], turbulence [2], aerosol and molecular scattering [3], thermal scattering due to heated aerosols, and aerosol heating and vaporization [4-7]. The relative importance of these processes depends on the parameters of the atmospheric environment which can vary significantly depending on location and time.

Atmospheric environments contain various types and concentrations of aerosol particles which can, for HEL beams, enhance thermal blooming and significantly affect the propagation efficiency. In general, aerosols consist of hygroscopic and non-hygroscopic particles of various sizes and chemical compositions. Hygroscopic aerosols are water-soluble and vary in size depending on the relative humidity [8]. Oceanic aerosols consist of sea salt, water, and organic material. Non-hygroscopic aerosols are composed of dust, soot, and other carbon-based compounds. These aerosols can have much larger absorption coefficients than water-based aerosols. While they are normally present in continental, rural and urban environments, dust aerosol particles can also be present in maritime environments hundreds of miles from shore [9].

Aerosols can absorb laser energy and, in the case of hygroscopic aerosols, the absorbed energy goes into both heating and vaporizing the aerosol. Heated aerosols conductively heat the surrounding air, resulting in an increase in thermal blooming of the HEL beam [10]. However, since aerosol scattering and absorption coefficients are strongly dependent on the aerosol particle radius, vaporizing the aerosol can improve the propagation efficiency. Non-hygroscopic aerosols (dust, etc.), however, have large scattering and absorption coefficients and will not vaporize at the intensity levels anticipated in DE applications. These aerosols continually heat the surrounding air leading to significant thermal blooming.

Water vapor absorption bands and those of carbon dioxide mainly determine the atmospheric transmission windows in the infrared. Under a range of atmospheric

conditions and laser wavelengths, aerosol absorption can exceed water vapor absorption and thus can be the dominant process for thermal blooming. For example, in a maritime environment at an operating wavelength of $\lambda = 1.045 \mu\text{m}$, the water vapor absorption coefficient is $\sim 3 \times 10^{-5} \text{ km}^{-1}$ [11] while the aerosol absorption coefficient is often greater than 10^{-3} km^{-1} . In other water vapor transmission windows, i.e., $1.625 \mu\text{m}$ and $2.141 \mu\text{m}$, the water vapor and aerosol absorption coefficients can be comparable. In addition to enhancing thermal blooming, aerosols can also significantly contribute to the total laser scattering coefficient.

In this study, the Advanced Navy Aerosol Model (ANAM) is used to model the near-surface maritime environment [12]. The ANAM aerosol distribution is comprised of various modes which represent aerosol particles of different compositions and sizes. Using Mie cross-sections, we calculate the absorption and scattering coefficients associated with each individual mode. The gross scattering and absorption coefficients that we obtain are comparable with *in situ* measurements [13,14].

In this report, we analyze the relevant processes which limit HEL propagation efficiency in maritime, desert, rural, and urban environments. To simulate the many inter-related processes affecting atmospheric HEL propagation, we use the **H**igh **E**nergy **L**aser **C**ode for **A**tmospheric **P**ropagation HELCAP [15], developed at the Naval Research Laboratory. HELCAP models, among others, the effects of i) aerosol and molecular scattering, ii) aerosol heating and vaporization, iii) thermal blooming due to both aerosol and molecular absorption, iv) atmospheric turbulence, and v) laser beam quality. It is the first HEL propagation model which integrates all these physical processes in a fully three-dimensional, time-dependent manner. In modeling the aerosol effects, we account for the aerosol distribution and the various aerosol modes (water-based, dust, soot, etc.). Furthermore, since the thermal blooming process is modeled in a fully time-dependent manner, we can simulate propagation through stagnation zones, i.e., locations at which the wind/slew velocity is zero [16].

In Section II we estimate the relative contributions to laser beam spreading and intensity loss in a maritime environment for three wavelengths lying within the water vapor transmission window. The effects considered include: laser beam quality effects, turbulence, molecular and aerosol thermal blooming, and aerosol thermal scattering,

molecular and aerosol scattering and absorption. In Section III, the various aerosol models, e.g., the Navy Aerosol Model (NAM) [17,18], the Advanced Navy Aerosol Model (ANAM) [12], the NRL Aerosol Analysis and Prediction System (NAAPS) [9], and our method for obtaining aerosol scattering and absorption coefficients are discussed. In Section IV, aerosol heating and vaporization and their effect on propagation are analyzed. Thermal blooming in the presence of aerosols is analyzed in Section V. In Section VI, the laser power delivered to a distant target as a function of transmitted laser power is found for a number of wavelengths and atmospheric environments. We show, among other things, that i) water vapor transmission windows are not necessarily the determining factor for choosing the optimum HEL wavelength ii) thermal blooming due to aerosol absorption can be the main contributor to beam spreading within the water vapor transmission windows iii) non-hygroscopic aerosols, because of their large absorption coefficient, and the fact that they can not be vaporized, are the main sources of aerosol absorption and hence thermal blooming and iv) moderate values of beam quality ($M^2 < 4$) have a minor effect on the propagation efficiency compared to the effects of turbulence, thermal blooming, and aerosol scattering.

Stagnation zones can be detrimental to HEL propagation since, without an effective clearing mechanism for the heated air, the strength of the thermal lens grows in time. In this situation, the defocusing process is eventually limited by thermal conduction or buoyancy. However, by the time these processes become effective, the beam may have already been severely degraded.

Thermal blooming in the presence of a stagnation zone was experimentally observed in a laboratory experiment using a 10W, CO₂ laser passed through an absorption cell containing CO₂ gas. The cell was pivoted to simulate a wind profile containing a stagnation zone. This experiment was also modeled using a code that solved time-dependent thermal blooming equations in the isobaric regime [16].

We examine the effect of a stagnation zone on a HEL beam focused onto a remote target in a maritime atmosphere. We first analyze the effect of a stagnation zone on the propagation of a focused beam and calculate an approximate expression for the relative intensity (Strehl ratio) on target as a function of focusing geometry and stagnation zone position. We then utilize the HELCAP code [28] to examine the propagation of a

megawatt-class HEL beam through a maritime atmosphere which contains a stationary stagnation zone along the laser path. The laser target configuration used in these simulations is shown in Fig. 1. We use the simulations to calculate the laser power delivered to a remote target for different wind profiles which place the stagnation zone at different locations along the laser propagation path.

II. Physical Processes Affecting HEL Propagation

The purpose of this section is to obtain *estimates* for the relative importance of the various physical processes that lead to transverse spreading and loss of intensity of an HEL beam. Three different laser wavelengths, $\lambda = 1.045, 1.625$ and $2.141\mu\text{m}$, all of which lie within water vapor transmission windows, are used for illustration. Full scale simulations of these interrelated processes will be presented and discussed in Sec. VI for a number of atmospheric environments. In this section we estimate these effects individually in order to better understand the results of the full scale simulations.

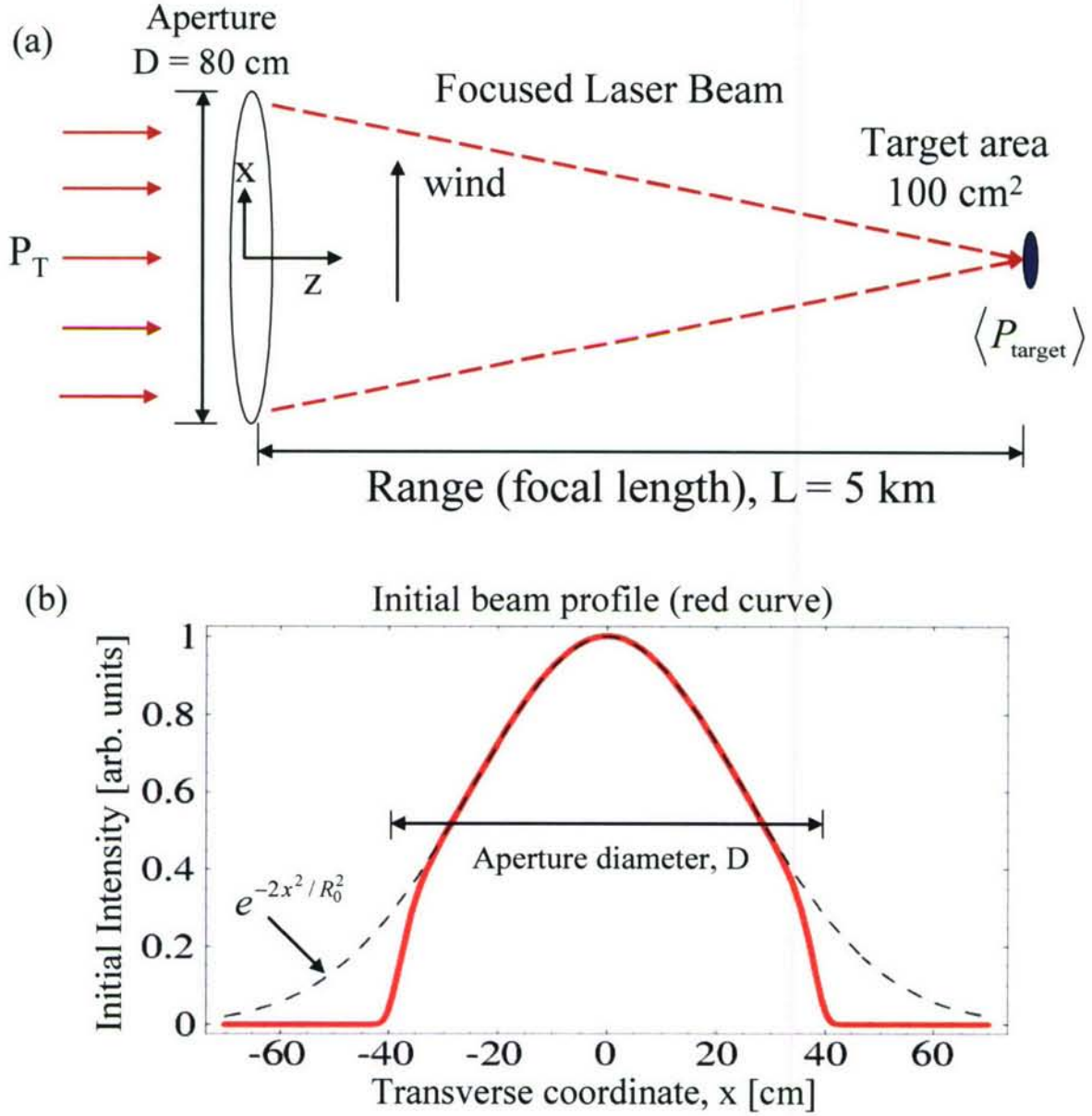


Figure 1: (a) Schematic of laser and target configuration used in illustration and full scale simulations. (b) Initial transverse intensity profile of the apertured laser beam (red curve) used in the simulations with $D = 80$ cm and $R_0 = 50$ cm. For comparison, the dashed curve denotes a Gaussian beam.

Laser Wavelengths, λ [μm]	1.045, 1.625, 2.141
Laser Power, P_T [MW]	1
Laser Spot size, R_0 [cm]	50
Aperture Diameter, D [cm]	80
Peak Laser Intensity at Source, I [kW/cm ²]	0.27
Average Intensity along Path, $\langle I \rangle$ [kW/cm ²]	2
Pointing Jitter, $\Delta\Theta_{jitter}$ [μ rad]	2
Laser Beam Quality, M^2	4
Target Range, L [km]	5
Wind Velocity, V_w [m/sec]	5
Turbulence Strength, C_n^2 [$m^{-2/3}$]	10^{-15}
Water Vapor Absorption Coefficient, α_{wv} [km ⁻¹]	3×10^{-5} , 2×10^{-3} , 3×10^{-3}
Aerosol Scattering Coefficient, β_A [km ⁻¹]	1.2×10^{-1} , 7×10^{-2} , 5×10^{-2}
Aerosol Absorption Coefficient, α_A [km ⁻¹]	2×10^{-3} , 2×10^{-3} , 3×10^{-3}
Effective Aerosol Absorption Coefficient, [km ⁻¹]	1×10^{-3}

Table 1: Laser and atmospheric parameters used in illustration to estimate and compare various effects

The configuration used in the HEL propagation examples is shown in Fig. 1. An HEL beam, with an aperture diameter of 80 cm, is focused onto a target a distance of $L \sim 5$ km from the source. For illustrative purposes, we chose atmospheric parameters typical of a maritime environment. The formulas used in the illustration, however, can be applied to other atmospheric conditions. The HEL and atmospheric parameters are listed in Table 1, for three laser wavelengths.

The average laser power on the target is determined by the change in the laser spot size on target and intensity loss due to the various processes. Some processes, e.g. turbulence, are due to small angle scattering events and for our purposes are best described by a laser beam spreading angle. The HEL spreading angle is the ratio of the change in spot size to the propagation distance, i.e., $\Delta\Theta \sim \Delta R / L$. Other processes, such as molecular scattering, result in large angle scattering events and are best described by an extinction coefficient.

i) Beam Quality

It is common practice to characterize the higher order modal content of a laser beam by a beam quality parameter denoted by M^2 . The quantity $M^2 \geq 1$ is a “times diffraction-limited” parameter which, for a fundamental Gaussian beam, is unity. This is one of many measures of beam quality and has a limited value in determining the far field profile. The laser spot size on the target due to finite beam quality, i.e., $M^2 = 4$, diffractive spreading is

$$\Delta R_{\text{quality}} \approx \frac{M^2 \lambda}{\pi R_0} L \approx \begin{cases} 1.1 \text{ cm, for } 1.045 \mu\text{m} \\ 1.7 \text{ cm, for } 1.625 \mu\text{m} \\ 2.2 \text{ cm, for } 2.141 \mu\text{m} \end{cases} \quad (1)$$

ii) Turbulence

Temperature and density fluctuations inherent in the atmosphere lead to random fluctuations in the refractive index. The resulting turbulence causes the laser beam to transversely spread and wander. The size distribution of the turbulence is often modeled

by a Kolmogorov distribution with structure function parameter C_n^2 , which characterizes the strength of the turbulence [2]. The increase of the laser beam spot size on the target due to turbulence is given by

$$\Delta R_{turb} \approx 2 \left(\frac{C_n^2 L}{\lambda^{1/3}} \right)^{3/5} L \approx \begin{cases} 2.6 \text{ cm, for } 1.045 \mu\text{m} \\ 2.4 \text{ cm, for } 1.625 \mu\text{m} \\ 2.3 \text{ cm, for } 2.141 \mu\text{m} \end{cases} \quad (2)$$

Note that the radial spread, ΔR_{turb} , is weakly dependent on the wavelength, i.e., is proportional to $\lambda^{-1/5}$.

iii) *Molecular scattering*

The ratio of the laser intensity on a target at range L to that at the source, due to molecular scattering, is

$$I_{\text{target}} / I_{\text{source}} = \exp(-\beta_m L). \quad (3)$$

The molecular scattering coefficient β_m can be written as

$$\beta_m = n_m \sigma_m \approx \begin{cases} 7.5 \times 10^{-4} \text{ km}^{-1}, \text{ for } 1.045 \mu\text{m} \\ 1.3 \times 10^{-4} \text{ km}^{-1}, \text{ for } 1.625 \mu\text{m} \\ 4.3 \times 10^{-5} \text{ km}^{-1}, \text{ for } 2.141 \mu\text{m} \end{cases} \quad (4)$$

where n_m is the molecular density and

$\sigma_m = (8\pi/3) \left(\pi (n_0^2 - 1) / n_m \lambda^2 \right)^2 \approx 3.3 \times 10^{-28} / \lambda^4 (\mu\text{m})$ is the Rayleigh scattering cross-section. The laser intensity loss due to molecular scattering is negligible,

i.e., $I_{\text{target}} / I_{\text{source}} = \exp(-\beta_m L) \approx 1$, for all three wavelengths.

iv) *Aerosol scattering*

The aerosol scattering coefficient is $\beta_A = \int dR F(R) \sigma_{\text{scat}}(R)$, where $F(R)$ is the aerosol particle radius distribution function and $\sigma_{\text{scat}}(R)$ is the scattering cross-section of an aerosol particle with radius R . The ratio of the laser intensity on a target at range L to that at the source is

$$I_{\text{target}} / I_{\text{source}} = \exp(-\beta_A L) \approx \begin{cases} 0.5, & \text{for } 1.045 \mu\text{m} \\ 0.7, & \text{for } 1.1625 \mu\text{m} . \\ 0.8, & \text{for } 2.141 \mu\text{m} \end{cases} \quad (5)$$

Aerosol scattering leads to significant loss of intensity, particularly at the shortest wavelength.

v) *Aerosol thermal scattering*

Aerosols absorb laser energy and heat the surrounding air through thermal conduction. The increase in air temperature has a spatially fluctuating component which can scatter the HEL beam. The uniformly heated component of the air temperature results in thermal blooming and is discussed in subsection vii). In the geometric optics limit, multiple, small-angle scatterings result in the spreading of the laser beam. The increase in the laser spot size on the target due to aerosol thermal scattering is given by

$$\Delta R_{A,T} \approx \Theta_{A,T} L$$

$$\approx 6.3 \times 10^{-4} \left(\frac{\alpha_D \langle I \rangle}{\kappa T_{\text{amb}} (1 + \varepsilon)} \right) n_A^{1/2} R_A^3 L^{3/2} \approx \begin{cases} 0.16 \text{ cm}, & \text{for } 1.045 \mu\text{m} \\ 0.57 \text{ cm}, & \text{for } 1.625 \mu\text{m} \\ 1.1 \text{ cm}, & \text{for } 2.141 \mu\text{m} \end{cases} , \quad (6)$$

where $\Theta_{A,T}$ is the spreading angle associated with thermal scattering, $\langle I \rangle$ is the average laser intensity along the propagation path, T_{amb} is the ambient air temperature, n_A is the number density of aerosols, R_A is the aerosol particle radius, α_D is the bulk absorption coefficient of the aerosols and ε is a constant of order unity representing the ratio of laser energy going into vaporization to laser energy conducted into the air. In obtaining the results in Eq. (6) the following values were used, $\alpha_D = 8.4, 30$ and 59 cm^{-1} for $1.045 \mu\text{m}$, $1.625 \mu\text{m}$ and $2.141 \mu\text{m}$, respectively.

vi) *Thermal blooming due to water vapor absorption*

Molecular absorption, particularly water vapor absorption, heats the air in the path of the HEL beam and results in thermal blooming. The molecular absorption coefficient is minimized by operating within the water vapor transmission window. The estimates in

this and the following subsection apply to *whole beam thermal blooming* in the steady state isobaric regime. A rough estimate for the increase in spot size on the target is

$$\Delta R_{TB, WV} \approx \gamma_{TB} \alpha_{WV} \langle I \rangle \frac{L^2}{V_W} \approx \begin{cases} 0.23 \text{ cm, for } 1.045 \mu\text{m} \\ 15.0 \text{ cm, for } 1.625 \mu\text{m} , \\ 22.5 \text{ cm, for } 2.141 \mu\text{m} \end{cases} \quad (7)$$

α_{WV} is the water vapor absorption coefficient,

$\gamma_{TB} = (n_0 - 1) / \rho_0 c_p T_0 = 7.5 \times 10^{-4} \text{ cm}^3/\text{J}$ at STP, V_W is the wind/slew velocity, and c_p , ρ_0 and T_0 are the specific heat at constant pressure, mass density and temperature of air, respectively. In obtaining Eq.(7) we used the whole beam thermal blooming defocusing angle $\Theta_{TB} \approx (\delta n_{TB} / R_o) L \approx (n_o - 1)(\delta \rho / \rho_o) L / R_o$ where δn_{TB} ($\delta \rho$) is the variation across the beam in the refractive index (air mass density) due to thermal blooming as discussed in Sec. V. It should be noted that in the presence of wind or slew the transverse intensity profile of the laser beam becomes highly asymmetric, i.e., crescent-shaped, and the above estimate for the spot size is merely an indication of the transverse scale associated with the intensity profile.

vii) *Aerosol-induced thermal blooming*

In addition to the thermal scattering effect discussed above, a collection of heated aerosol particles can also lead to enhanced thermal blooming [10]. Aerosol-induced thermal blooming is due to thermal conduction from the heated aerosols into the surrounding air. The effective absorption coefficient for aerosol-induced thermal blooming is given by $\alpha_A / (1 + \varepsilon)$ where α_A is the aerosol absorption coefficient. The increase in the laser beam spot size on the target due to aerosol-induced thermal blooming is approximately

$$\Delta R_{TB, A} \approx \frac{\alpha_A}{1 + \varepsilon} \gamma_{TB} \langle I \rangle \frac{L^2}{V_W} \approx \begin{cases} 4.7 \text{ cm, for } 1.045 \mu\text{m} \\ 4.7 \text{ cm, for } 1.625 \mu\text{m} . \\ 7 \text{ cm, for } 2.141 \mu\text{m} \end{cases} \quad (8)$$

Aerosol induced thermal blooming will be discussed in detail in Sec. V.

The contributions to the laser spot size and loss in laser intensity on target due to the various processes described above are summarized in Table 2. The laser and atmospheric parameters used in these examples are listed in Table 1 for three

wavelengths which lie within the water vapor transmission windows. The contribution to the spot size increase due to beam jitter, $\Delta R_{jitter} \sim \Delta \Theta_{jitter} L \sim 1 \text{ cm}$, is the same for the three wavelengths. Molecular (Rayleigh) scattering is practically negligible in the three cases.

Based on the above illustration we find that: i) for a laser wavelength of $1.045 \mu\text{m}$ the spread in the beam spot size is dominated by aerosol induced thermal blooming, while the intensity on target is reduced by almost 50% as a result of aerosol scattering, ii) for a laser wavelength of $1.625 \mu\text{m}$ thermal blooming due to water vapor absorption is the dominant contributor to the spread in the beam spot size, while the intensity on target is reduced by nearly 30% as a result of aerosol scattering, iii) for the case of $2.141 \mu\text{m}$ thermal blooming due to water vapor absorption is by far the largest contributor to the spread in the beam spot size, while the intensity on target is reduced by nearly 20% as a result of aerosol scattering and finally, iv) moderate values of the laser beam quality factor M^2 , i.e., values less than 4, have little effect on the propagation of HELs compared to molecular/aerosol thermal blooming effects or turbulence.

Comparing the three wavelengths considered in Tables 1 and 2, aerosol scattering is more important for the shortest wavelength, $1.045 \mu\text{m}$, while water vapor induced thermal blooming is an issue for the longest wavelength, $2.141 \mu\text{m}$. As far as the loss in intensity due to scattering is concerned, $2.141 \mu\text{m}$ results in the largest propagation efficiency. It should be noted, however, that the results given in Table 2 are meant to be illustrative, and not necessarily typical of a maritime atmosphere.

III. Atmospheric Aerosols

As shown in the previous Section, aerosol scattering and absorption can play an important role in limiting the laser energy delivered to a remote target. In typical maritime and continental environments, the aerosol scattering and absorption coefficients can be as large as 0.2 km^{-1} and 0.01 km^{-1} , respectively, even though the average water content of aerosols is typically far less than that of humid air. For example, at a temperature of 30°C and relative humidity of 50%, the water vapor mass density is $\rho_{wv} \sim 1.5 \times 10^{-5} \text{ g/cm}^3$ while the average mass density of maritime aerosols is typically

Wavelength, λ [μm]	1.045	1.625	2.141
Beam Quality, $\Delta R_{\text{quality}}$ [cm]	1.1	1.7	2.2
Beam Jitter, ΔR_{jitter} [cm]	1	1	1
Turbulence, ΔR_{turb} [cm]	2.6	2.4	2.3
Water Vapor, Thermal Blooming, $\Delta R_{\text{TB},\text{WV}}$ [cm]	0.23	15	22.5
Aerosol Thermal Scattering, $\Delta R_{\text{A},\text{T}}$ [cm]	0.16	0.57	1.1
Aerosol Induced Thermal Blooming, $\Delta R_{\text{TB},\text{A}}$ [cm]	4.7	4.7	7
Intensity Ratio (Molecular Scattering), $I_{\text{target}} / I_{\text{source}}$	1	1	1
Intensity Ratio (Aerosol Scattering), $I_{\text{target}} / I_{\text{source}}$	0.5	0.7	0.8

Table 2. Estimates of HEL spreading and intensity loss due to various processes for three laser wavelengths

far less, $\leq 10^{-9} \text{ g/cm}^3$. However, water molecules scatter more efficiently in the form of aerosols due to the collective nature of the scattering.

Aerosol particles occur over a range of sizes and compositions. Maritime aerosols consist of seawater droplets with radii in the range $0.01 \mu\text{m} - 10 \mu\text{m}$ [17]. Continental aerosols are typically comprised of soot and non-hygroscopic dust, biomass smoke, and a variety of water-soluble materials [9]. There are numerous models that attempt to describe the size distribution and composition of aerosols. The Navy Aerosol Analysis and Prediction System (NAAPS) is a near-operational predictive aerosol model that uses meteorological data from the Navy Operational Global Atmospheric Prediction System (NOGAPS) to forecast aerosol concentrations in real time. It has extensive microphysics and chemistry models and includes dust, sulfur, and smoke simulations. The Coupled Ocean-Atmosphere Mesoscale Prediction System (COAMPS) is a regional model that works in conjunction with NAAPS and provides the vertical distribution of aerosol particles [9]. Presently, however, NAAPS and COAMPS have not been applied to specific near-surface scenarios of interest for HEL applications.

The Navy Aerosol Model (NAM) [17,18] and its successor, the Advanced Navy Aerosol Model (ANAM) [12] are used to model near-surface maritime environments. While ANAM has been benchmarked in near-surface open-ocean conditions, it may not accurately represent the detailed composition and distribution of aerosol particles in regions where dust aerosols are expected to be present [9]. Nevertheless, ANAM can generate reasonable gross scattering and absorption coefficients which are sufficient for our purposes of simulating aerosol induced thermal blooming and laser scattering. In this study, we will use ANAM to generate the maritime aerosol scattering and absorption coefficients used in our simulations.

The “Navy Maritime” aerosol model of the MODTRAN atmospheric transmission code [19] uses NAM, but neglects the dust contribution, i.e., mode 0. Thus, it cannot be used to accurately describe near-shore maritime environments. The default MODTRAN “Maritime” aerosol model, however, gives aerosol absorption coefficients ($\sim 10^{-3} \text{ km}^{-1}$) that are similar to ANAM results for polluted coastal environments.

Mode	Material	R_{A0} [μm]	$\text{Re}(n)$	$\text{Im}(n)$
0	Non-hygroscopic dust	0.03	1.52	8×10^{-3}
1	Water soluble + water	0.03	1.37	9.6×10^{-5}
2	Sea salt + water ("aged" aerosol)	0.24	1.38	6.9×10^{-5}
3	Sea salt + water (new aerosol)	2	1.37	6.5×10^{-5}
4	Sea salt + water (near-surface)	8	1.37	6.5×10^{-5}

Table 3: Aerosol material composition, mean radius, and refractive index of the various ANAM aerosol modes for $\text{RH} = 80\%$, $U_{10} = U_{24} = 5$ m/sec, $\text{AMP} = 8$, $h = 5$ m, $\lambda = 1.045 \mu\text{m}$.

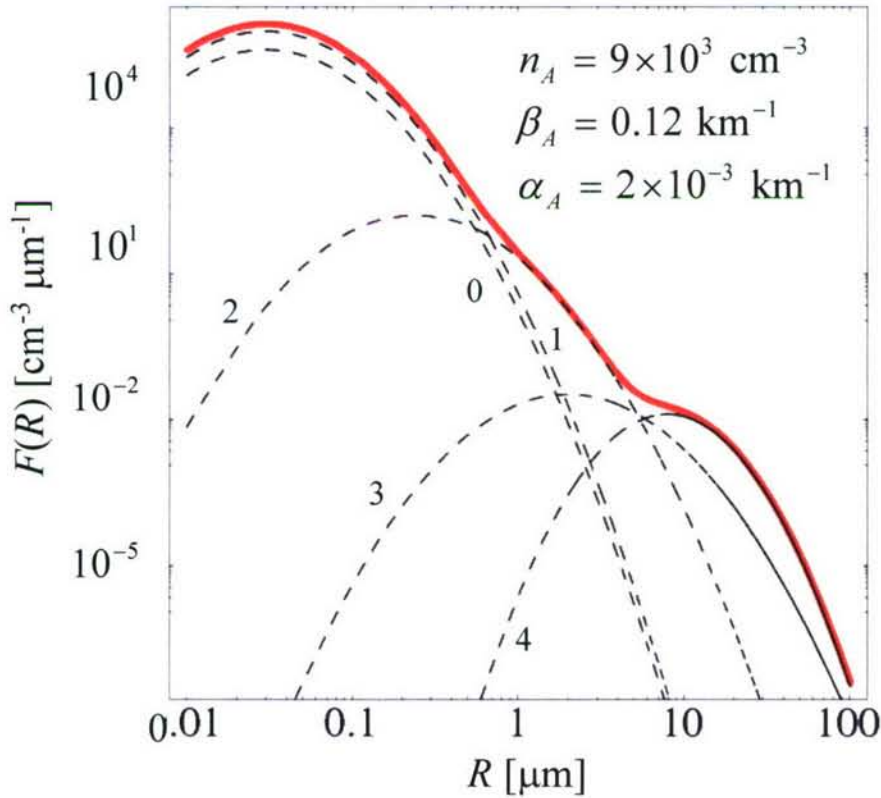


Figure 2: Aerosol distribution function calculated according to ANAM 3.0. Dashed curves denote individual aerosol modes 0-4. Solid curve denotes the total aerosol distribution function. $\text{RH} = 80\%$, $U_{10} = U_{24} = 5$ m/sec, $\text{AMP} = 8$, $h = 5$ m, $\lambda = 1.045 \mu\text{m}$.

The ANAM aerosol particle distribution is comprised of various modes which represent aerosol particles of different compositions and sizes. These aerosol modes will absorb laser energy and vaporize at different rates. The aerosol particle size distribution function, $F(R) = \sum_{j=0}^4 F_j(R)$, where R is the aerosol particle radius, is represented as a superposition of five “modes” with each mode representing aerosols with a particular physical composition and origin. The total aerosol density is given by $n_A = \int dR F(R)$. Mode 0 represents dust particles of continental origin, mode 1 represents water-soluble aerosols, and modes 2-4 represent marine aerosols (sea salt and water) that result from different processes. NAM contains only modes 0 - 3. The physical properties of the various modes are summarized in Table 3. Each mode is described by a lognormal distribution over aerosol particle radius with a characteristic amplitude and width. The mean radius and distribution width of the water-based modes (1-4) are related to the ambient relative humidity (RH) using the model of Gerber [20]. The amplitude of modes 2 and 3 are related to the 24 hour averaged wind speed (U_{24}) and instantaneous wind speed at 10m altitude (U_{10}), respectively. The amplitude of mode 4 is related to the height above the sea surface (h) through an empirically determined relation. The air mass parameter (AMP) controls the amplitudes of modes 0 and 1. AMP is a dimensionless parameter varying between 1 (open ocean) and 10 (highly polluted coastal area) that qualitatively characterizes the amount of dust or continental aerosols in the atmosphere. However, it is not directly related to any measured meteorological parameter and can be varied somewhat arbitrarily to produce scattering coefficients that agree with measurements. As such, ANAM has no real predictive capability in regions where dusty aerosols are expected to play an important role. Figure 2 plots the ANAM aerosol distribution function for the various modes for RH = 80%, $U_{10} = U_{24} = 5$ m/sec, AMP = 8, and $h = 5$ m.

Calculation of the aerosol scattering and absorption coefficients also requires that the complex refractive index of the various aerosol modes and the complex cross section of the aerosol droplets, $\sigma = \sigma_{scat} + i \sigma_{abs}$, be known. Here, we take the refractive index

Maritime Environment (ANAM)			
Mode	Density [cm^{-3}]	β_A [km^{-1}]	α_A [km^{-1}]
0	2.6×10^3	0.028	1.6×10^{-3}
1	6.1×10^3	0.038	4.2×10^{-5}
2	9.0	0.032	3.2×10^{-5}
3	0.014	2.9×10^{-3}	2.4×10^{-5}
4	0.014	0.016	2.2×10^{-4}
Total	9×10^3	0.12	2×10^{-3}

Table 4: Aerosol number density, n_A , scattering coefficient, β_A , and volumetric absorption coefficient, α_A , associated with the various ANAM aerosol modes for the same parameters as used for Fig. 2, i.e., $\text{RH} = 80\%$, $U_{10} = U_{24} = 5$ m/sec, $\text{AMP} = 8$, $h = 5$ m, $\lambda = 1.045 \mu\text{m}$.

of dust from Shettle and Fenn [21], sea salt and water-soluble materials are taken from from Volz [22, 23], and pure water from Hale and Query [24]. These indices are also tabulated in the technical documentation for NAM [18]. For modes 1-4 (hygroscopic aerosols) the refractive index is also a function of relative humidity. The values for n given in Table 3 are calculated for RH = 80 % [18]. The complex cross sections are calculated according to Mie theory. We use MODTRAN to calculate the molecular absorption and scattering coefficients [19].

Since the aerosol distribution can evolve with time, due to vaporization for example, the aerosol absorption and scattering coefficients are also time-dependent and given by

$$\alpha_A(t) = \int \sum_{j=0}^4 \sigma_{abs,j}(R) F_j(R,t) dR, \quad (9a)$$

$$\beta_A(t) = \int \sum_{j=0}^4 \sigma_{scat,j}(R) F_j(R,t) dR, \quad (9b)$$

where the scattering and absorption cross sections are $\sigma_{scat,j} = \pi R^2 Q_{scat,j}$ and $\sigma_{abs,j} = \pi R^2 Q_{abs,j}$, respectively, Q is the efficiency and j denotes mode number.

Table 4 lists the aerosol number density and scattering and absorption coefficients associated with each aerosol mode for the same parameters used in Fig. 2. For these parameters, mode 1 (water-soluble aerosols) has the largest number density. However, mode 0 has the largest absorption coefficient by far due to the large imaginary refractive index of dust-like aerosols. Mode 2 has the largest contribution to scattering. The total aerosol number density, scattering coefficient, and absorption coefficient associated with the distribution of Fig. 2 are given in Table 2, $n_A = 9 \times 10^3 \text{ cm}^{-3}$, $\beta_A = 0.12 \text{ km}^{-1}$, and $\alpha_A = 1.9 \times 10^{-3} \text{ km}^{-1}$, respectively. The corresponding visibility in this example is $\sim 3.9 / \beta_A \sim 32 \text{ km}$.

IV. Aerosol Heating and Vaporization

Scattering and blooming effects of aerosols can be reduced by vaporizing the water-based aerosols. The aerosol scattering and absorption coefficients are, in general,

functions of the size parameter $2\pi R_A / \lambda$. The aerosol absorption and scattering coefficient scales with aerosol particle radius as,

$$\alpha_A(t) \sim R_A^3(t), \quad (10a)$$

$$\beta_A(t) \sim \begin{cases} R_A^6(t), & \text{Rayleigh limit,} \\ R_A^2(t), & \text{Mie limit,} \end{cases} \quad (10b)$$

where the Rayleigh and Mie limits are defined as $2\pi R_A / \lambda \ll 1$ and $2\pi R_A / \lambda \gg 1$, respectively. Given the strong dependence of α_A and β_A on the aerosol particle radius, vaporization can reduce both the aerosol absorption and scattering coefficients. In the following we discuss the heating and vaporization of a single water-based aerosol droplet. We use these results to model the vaporization of a distribution of aerosol particles and the effect of vaporization on the atmospheric scattering and absorption coefficients.

i) Vaporization of an Aerosol Droplet

Heating and vaporization of a single water-based aerosol droplet are described by the following coupled equations for the aerosol particle temperature and radius [6],

$$\frac{\partial \Delta T_A}{\partial t} \approx \frac{\alpha_D I}{\rho_A c_A} + \frac{3 H_{vap}}{c_A R_A} \frac{\partial R_A}{\partial t} - \frac{3 \kappa}{\rho_A c_A R_A^2} \Delta T_A, \quad (11a)$$

$$\frac{\partial R_A}{\partial t} \approx -\frac{\alpha_s \Lambda}{R_A} \Delta T_A, \quad (11b)$$

where $\Delta T_A = T_A - T_{amb}$, T_A is the aerosol particle temperature, T_{amb} is the ambient air temperature, R_A is the aerosol particle radius,

$\alpha_D = \pi R_A^2 Q_{abs} / (4\pi R_A^3 / 3) = 3 Q_{abs} / 4 R_A$ is the bulk absorption coefficient of the aerosol droplet, $Q_{abs}(R)$ is the absorption efficiency, α_s is the evaporation coefficient (sticking fraction), ρ_A is the mass density of the droplet, κ is the thermal conductivity of air, c_A is the specific heat of the aerosol droplet, H_{vap} is the enthalpy of vaporization,

$\Lambda = m_v D_{air} p_o \xi \exp(-\xi) / \rho_A k_B T_{amb}^2$, $\xi = M_{vap} H_{vap} / R T_{amb}$, m_v is the weight of a vapor molecule, $D_{air} = 0.24 \text{ cm}^2/\text{sec}$ is the diffusion coefficient of air, k_B is the Boltzman constant, M_{vap} is the molecular vapor mass (e.g., $M_{vap} = 18$ for water vapor), $R = 8.3 \text{ J}/(\text{K} - \text{mol})$ is the universal gas constant and p_0 is the constant of integration (with units of pressure) in the Clausius-Clapeyron formula, evaluated here for a saturated (i.e., 100% RH) water vapor pressure of 2.34 kPa at the temperature of 293 K. The first term on the right hand side of Eq. (11a) represents the absorbed laser energy, the second term is due to vaporization and the third is due to thermal conduction into the surrounding air. The rate of change of the aerosol particle radius is given by Eq. (11b). Equations (11a) and (11b) are valid for $\xi \Delta T_A / T_A \ll 1$ and

$\tau_{vap} \equiv |\partial \ln R_A / \partial t|^{-1} \gg R_A^2 \rho_A c_A / \kappa$. For water at $T_{amb} = 293 \text{ K}$, $c_A = 4.2 \text{ J}/(\text{g} - \text{K})$, $\kappa = 2.5 \times 10^{-4} \text{ W}/(\text{cm} - \text{K})$, $H_{vap} = 2.3 \text{ kJ/g}$ and we find that $\xi = 17$,

$\Lambda = 2.4 \times 10^{-7} \text{ cm}^2/(\text{K} - \text{sec})$. For a water-based aerosol particle with $R_A = 1 \mu\text{m}$, Eqs.(11a) and (11b) are valid for vaporization times $\tau_{vap} \gg 0.1 \text{ msec}$. The bulk absorption coefficient for an oceanic aerosol droplet is $\alpha_D = 8.4, 30$ and 59 cm^{-1} at the wavelengths $\lambda = 1.045 \mu\text{m}$, $1.625 \mu\text{m}$, and $2.141 \mu\text{m}$, respectively. Convection of the aerosols across the laser beam due to a wind or slew limits the heating and vaporization time to the local clearing time. This effect is contained in the full-scale numerical simulations of Sec. VI.

The aerosol temperature increases due to the absorbed laser energy and cools due to vaporization and thermal conduction. In the adiabatic regime, where the heating and cooling terms on the right hand side of Eq. (11a) are balanced, the aerosol temperature is given by

$$\Delta T_A = \frac{\alpha_D I R_A^2}{3 \kappa (1 + \varepsilon)}, \quad (12)$$

where $\varepsilon = \alpha_s H_{vap} \rho_A \Lambda / \kappa$ is the ratio of the aerosol vaporization energy to the aerosol energy conducted into the air; i.e., ratio of the last terms in Eq.(11a) [5]. For water at an ambient temperature of $T_{amb} = 293 \text{ K}$, it is found that $\varepsilon = 2.2$. The adiabatic regime is

reached in a time on the order of the thermal conduction time given by

$\tau_{diff} = \rho_A c_A R_A^2 / (3\kappa(1 + \varepsilon))$. For an aerosol particle with $R_A = 1 \mu\text{m}$, the thermal conduction time is $\tau_{diff} \approx 20 \mu\text{sec}$. In the adiabatic limit and constant laser intensity the aerosol particle radius decreases exponentially with time according to

$$R_A(t) = R_{A0} \exp(-t / \tau_{vap}), \quad (13)$$

where R_{A0} is the initial radius of the aerosol particle and $\tau_{vap} = 3\rho_A H_{vap}(1 + \varepsilon^{-1})/(\alpha_D I)$ is the vaporization time.

Figure 3 plots the aerosol particle temperature and radius as a function of time as given by Eqs. (11a) and (11b). The laser intensity is taken to be $I = 2 \text{ kW/cm}^2$. Figure (3a) shows that the temperature increases for a time comparable with the thermal conduction time before reaching a maximum value which is well-approximated by Eq. (12). Figure (3b) shows the characteristic exponential decrease of the aerosol particle radius in time. Note that for these parameters the vaporization time is essentially independent of initial radius, as predicted by Eq. (13).

ii) *Vaporization of a Distribution of Aerosols*

Assuming that the radius of each individual aerosol particle undergoing vaporization evolves according to $R_A(t) = R_{A0} h(t)$, as in Eq. (13), it can be shown that the aerosol particle radius distribution function can be written as

$$F(R, t) = \frac{F_0(R/h(t))}{h(t)}, \quad (14)$$

where $F_0(R)$ is the initial distribution function. In the adiabatic limit described by Eq.

(14), each mode is characterized by $h_j(t) = \exp(-t / \tau_{vap,j})$, where

$\tau_{vap,j} = 3\rho_{A,j} H_{vap,j}(1 + \varepsilon_j^{-1})/(\alpha_{D,j} I)$, for $j = 1$ to 4. We assume that mode 0 (non-hygroscopic dust) does not vaporize. In general, α_D is weakly dependent on the particle radius. However, for the purpose of obtaining a vaporization time for each mode, we

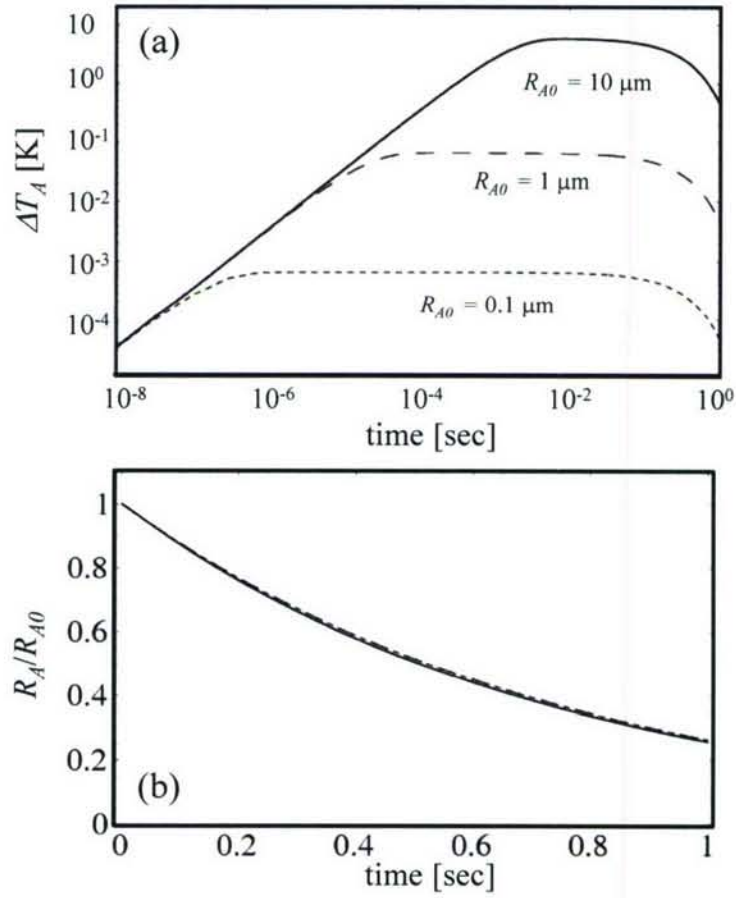


Figure 3: Aerosol temperature (a) and normalized radius (b) versus time for initial radii, $R_{A0} = 0.1, 1$, and $10 \mu\text{m}$, and $\alpha_D I = 14 \text{ kW/cm}^3$. Curves are almost indistinguishable in figure (b).

take $\alpha_{D,j} = 4\pi \text{Im}(n_j) / \lambda$, which is the absorption coefficient in the Rayleigh limit where n_j is the refractive index for aerosol mode j . For a constant laser intensity of $I = 2 \text{ kW/cm}^2$, the vaporization times associated with each mode are $\tau_{vap,1} = 0.42 \text{ sec}$, and $\tau_{vap,2} = \tau_{vap,3} = \tau_{vap,4} \approx 0.62 \text{ sec}$.

Figure 4 plots the total aerosol scattering and absorption coefficients versus time. The scattering coefficient is seen to decrease by a factor of 5 after $\sim 1 \text{ sec}$. The absorption coefficient is not decreased significantly due to the presence of non-hygroscopic aerosols (mode 0) which do not vaporize.

V. Thermal Blooming in the Presence of Aerosols

Propagation of a high energy laser beam in the atmosphere results in a small fraction of the laser energy being absorbed by both the molecular and aerosol constituents of air. The absorbed energy locally heats the air and leads to a decrease in the air density which modifies the refractive index, given by $\delta n_{TB} = (n_0 - 1)\delta\rho / \rho_0$, where ρ_0 and $\delta\rho$ are the ambient and perturbed air mass densities, respectively. The refractive index variation leads to a defocusing or spreading of the laser beam known as thermal blooming [1].

For an isobaric process the perturbed air temperature δT is related to the perturbed density by $\delta\rho = -(\rho_0 / T_0)\delta T$ and evolves in time according to

$$c_p \rho_0 \left(\frac{\partial}{\partial t} + \mathbf{V}_w \cdot \nabla - \frac{\kappa}{c_p \rho_0} \nabla^2 \right) \delta T = \alpha_{total} I, \quad (15)$$

where κ is the thermal conductivity, c_p is the specific heat of air at constant pressure, \mathbf{V}_w is the wind or slew velocity and I is the time-averaged laser intensity. The isobaric regime is valid for times greater than the hydrodynamic time R_L / C_s , where R_L is the laser spot size and C_s is the acoustic speed.

The rate of change of laser energy density absorbed in air determines the degree of thermal blooming and is given by the total absorption coefficient α_{total} ,

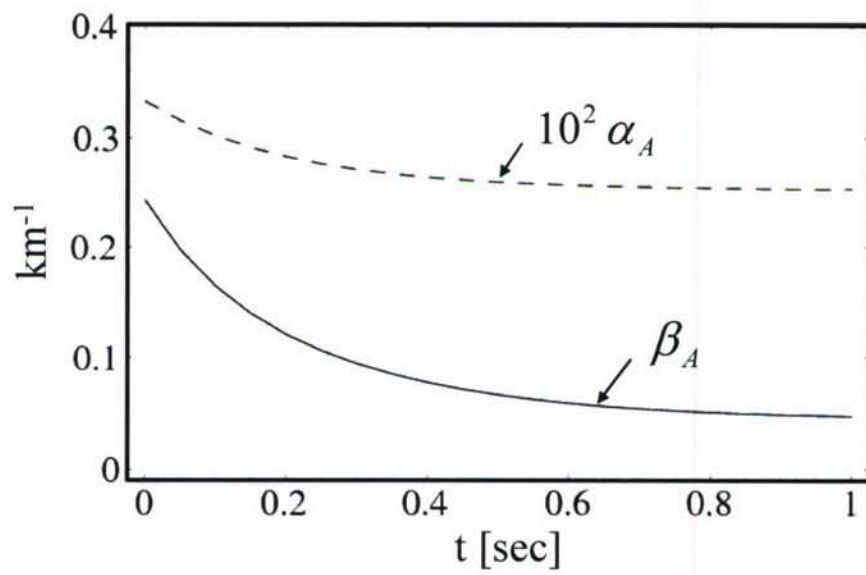


Figure 4: Aerosol absorption (dashed curve) and scattering coefficient (solid curve) for a distribution of aerosols versus time for a constant laser intensity, $I = 2 \text{ kW/cm}^2$. The initial aerosol distribution corresponds to that of Fig. 2.

$$\alpha_{total} I = \alpha_{WV} I + 4\pi\kappa n_A R_A \Delta T_A + \alpha_{WV} \frac{\rho_{WV}}{\rho_{WV,amb}} I + \frac{2\pi n_A \rho_A k_B \Delta T_A}{m_v} \frac{\partial R_A^3}{\partial t}, \quad (16)$$

where the first term on the right hand side is due to ambient water vapor absorption, the second is due to conductive heating of the air from the heated aerosols, the third is due to the additional water vapor from the vaporized aerosols, and the last term is due to the fact that water vapor from a vaporized aerosol enters the air at an elevated temperature. The third term is small compared to the first since $\rho_{WV} / \rho_{WV,amb} \ll 1$, and the ratio of the fourth to the second term is

$$\frac{3\rho_A k_B R_A}{2m_v \kappa} \frac{\partial R_A}{\partial t} = 0.2\alpha_s \Delta T_A / T_{amb} \ll 1.$$

Hence, the last two terms on the right side of Eq. (16) can be neglected.

A further simplification applies in the adiabatic regime where the temperature change is proportional to the laser intensity. Substituting Eq. (12) for ΔT_A into Eq. (16) results in the following thermal blooming absorption coefficient for a homogeneous aerosol distribution

$$\alpha_{total} = \alpha_{WV} + \frac{\alpha_D n_A}{1 + \varepsilon} \left(\frac{4\pi R_A^3}{3} \right). \quad (17)$$

The result in Eq.(17) is important because it shows that aerosol absorption, modified by vaporization, contributes directly to the thermal blooming absorption coefficient.

In general, for a non-homogeneous aerosol distribution, the last term in Eq.(17) must be averaged over the aerosol distribution to give $\alpha_{total} = \alpha_{WV} + \alpha_A / (1 + \varepsilon)$, where we have

used the definition of the aerosol absorption coefficient, $\alpha_A \equiv \int F(R) Q_{abs}(R) \pi R^2 dR$

where $Q_{abs}(R) = 4R\alpha_D(R)/3$ is the imaginary part of the scattering efficiency. For the multi-mode aerosol distribution of Fig. 2, Eq. (17) can be written as

$$\alpha_{total} = \alpha_{WV} + \sum_{j=0}^4 \frac{\alpha_{A,j}}{1 + \varepsilon_j}. \quad (18)$$

The aerosol contribution to the overall absorption coefficient can be much larger than that of molecular water vapor. For example, in the “water window” at wavelength $1.045\mu\text{m}$, $\alpha_{wv} = 3 \times 10^{-5} \text{ km}^{-1}$, while from Table 4 the effective aerosol contribution can be up to two orders of magnitude larger. When non-hygroscopic aerosols represent a large fraction of the aerosol population, it is not possible to significantly reduce the absorption coefficient by vaporization. Therefore, the optimum laser wavelength for reducing thermal blooming should not be primarily determined by the transmission windows of molecular water vapor, but must also consider the absorption and conductive air heating due to aerosols.

VI. Simulations of HEL Propagation

In this section we present results of full-scale computer simulations of HEL propagation through various atmospheric environments. The propagation code used for this study is HELCAP (High Energy Laser Code for Atmospheric Propagation) which is a fully time-dependent, 3D code developed at the Naval Research Laboratory [15].

HELCAP models the propagation of continuous and pulsed HELs through the atmosphere. Representing the laser electric field as

$\mathbf{E} = A(x, y, z, t) \exp[i(\omega_o z/c - \omega_o t)] \hat{\mathbf{e}}_x / 2 + c.c.$, where $\omega_o = 2\pi c/\lambda$ is the laser frequency, $\hat{\mathbf{e}}_x$ is a unit polarization vector in the x direction, $A(x, y, z, t)$ is the complex laser amplitude and the laser intensity is $I = c A A^* / 8\pi$. HELCAP solves a nonlinear Schrödinger-like equation which has the form

$$\frac{\partial A}{\partial z} = \frac{ic}{2\omega_o} \nabla_{\perp}^2 A + \left[i \frac{\omega_o}{c} (\delta n_T + \delta n_{TB}) - \frac{1}{2}(\alpha + \beta) \right] A + \sum_j S_j, \quad (19)$$

where $\alpha = \alpha_m + \alpha_A$ is the total absorption coefficient, $\beta = \beta_m + \beta_A$ is the total scattering coefficient, and δn_T and δn_{TB} denote the refractive index variation due to atmospheric turbulence and thermal blooming respectively. α_m (α_A) is the molecular (aerosol) absorption coefficient. β_m (β_A) is the molecular (aerosol) scattering coefficient. The quantities δn_T , δn_{TB} , α , and β are space and time-dependent and determined self-consistently in the presence of the effects discussed in the previous

sections, e.g., aerosol heating and vaporization. The effects of wind or beam slew, on the air and aerosol heating is contained in the full scale simulations presented in this Section.

The terms denoted by $\sum_j S_j$ represent other physical processes such as group velocity dispersion, ionization, relativistic effects, nonlinear Kerr effects, and stimulated Raman scattering. While these processes do not significantly affect the propagation of the HEL beams considered here, they are important for the propagation of ultra-high intensity femtosecond laser pulses [25, 26].

In the following examples, we consider the propagation of HEL beams in i) maritime, ii) desert, iii) rural, and iv) urban atmospheres. In these examples, the laser wavelengths are taken to be $1.045\text{ }\mu\text{m}$, $1.625\text{ }\mu\text{m}$, and $2.141\text{ }\mu\text{m}$, which correspond to atmospheric transmission windows, i.e., minima in molecular (water vapor) absorption. HELCAP requires the initial scattering and absorption coefficients associated with vaporizable (water-based) and non-vaporizable (e.g., dust, soot) aerosol constituents as inputs. For the maritime atmosphere we use ANAM to generate the aerosol scattering and absorption coefficients. For the urban, rural, and desert environments we use MODTRAN4 and the Air Force Geophysics Laboratory (AFGL) model of Ref. [27] to generate the aerosol parameters. MODTRAN4 yields the overall aerosol scattering and absorption coefficients while the AFGL model gives the physical compositions and percentages of vaporizable and non-vaporizable aerosols.

The propagation configuration is shown in Fig.1. The high energy laser beam has an initial field profile given by $A = A_0 f(r) g(t) \exp(-r^2 / R_0^2)$, where $f(r) = \exp[-(2r / D)^\ell]$, $\ell = 20$, limits the transverse extent of the beam to the aperture diameter, D , and $g(t)$ is the initial temporal profile of the beam. The transmitted power at the source is denoted by P_T . The laser is focused onto a remote target at a range of 5 km. The target is taken to be circular with an area of 100 cm^2 . The propagation direction is along the z-axis and a uniform transverse wind, with velocity $V_w = 5\text{ m/sec}$ is directed along the y-axis. Atmospheric turbulence is modeled by a Kolmogorov spectrum with structure constant $C_n^2 = 10^{-15}\text{ m}^{-2/3}$. The pointing jitter associated with the laser beam is

taken to have an angular spread of 2 μrad and a white noise temporal spectrum. Since thermal blooming and turbulence can cause the laser beam centroid to wander, adaptive optics techniques are employed to keep the laser beam centered on the target. In the simulations, the target is always located such that the peak laser fluence at 5 km range is at the center of the target.

The average power on target is used as a figure of merit in the following examples. It is defined by

$$\langle P_{\text{target}} \rangle = \frac{1}{\tau_{\text{dwell}}} \int_0^{\tau_{\text{dwell}}} d\tau \int dx dy I(x, y, z = L, \tau), \quad (20)$$

where the dwell time $\tau_{\text{dwell}} = 1 \text{ sec}$, and $dx dy$ is the differential cross section which is integrated over the target area. The total laser energy reaching the target is

$E_{\text{target}} = \langle P_{\text{target}} \rangle \tau_{\text{dwell}}$. However, this laser energy is not necessarily absorbed by the target. Calculation of the absorbed laser energy requires additional information such as the target material absorption coefficient, surface roughness, surface curvature, etc, which is not considered here.

i) Maritime Environment

The maritime environment is characterized by a mixture of salt water aerosols, water soluble aerosols and dust aerosols, as described in Sec. III. In this example we use the aerosol distribution shown in Fig. 2 to calculate the scattering and absorption coefficients. These coefficients, as well as the molecular absorption coefficients, are listed in Table 1. For the vaporization calculations, we assume droplet absorption coefficient of $\alpha_D = 8 \text{ cm}^{-1}$, 30 cm^{-1} , and 59 cm^{-1} for the wavelength $\lambda = 1.045 \mu\text{m}$, $1.625 \mu\text{m}$, and $2.141 \mu\text{m}$, respectively. These values are calculated assuming 80% RH and using the refractive index for oceanic aerosols [18].

Figure 5 plots the average power on target versus the transmitted power, P_T , for the three wavelengths of interest. Our results show that for a maritime environment, the optimum wavelength depends on the transmitted power. For $P_T < 1.5 \text{ MW}$, propagation is mostly affected by aerosol scattering and the average power on target increases with

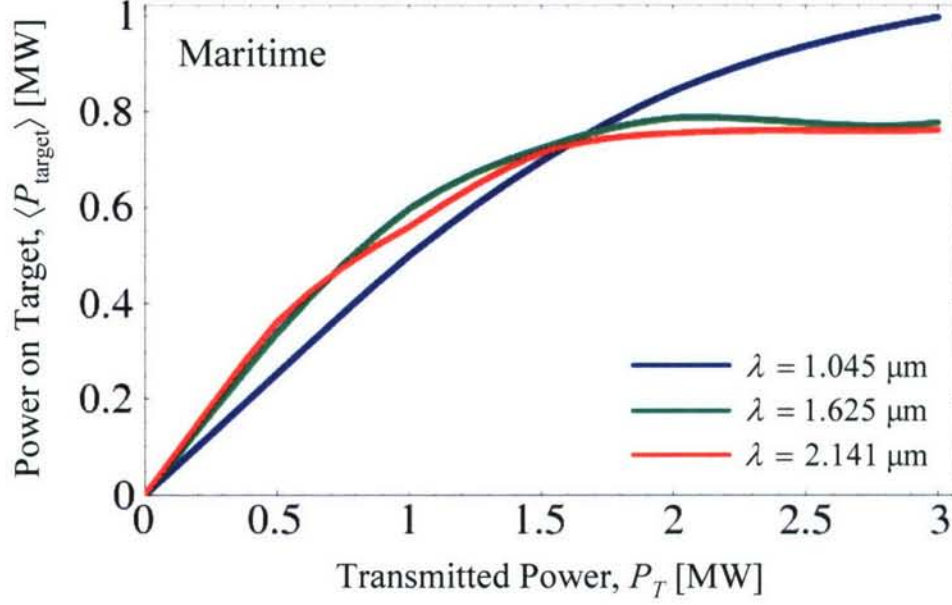


Figure 5: Average power on target, $\langle P_{\text{target}} \rangle$, versus transmitted power, P_T , in a maritime environment for the wavelengths $\lambda = 1.045, 1.625, 2.141 \mu\text{m}$. Initial beam profile has $R_0 = 50 \text{ cm}$, $D = 80 \text{ cm}$. Simulation geometry is shown in Fig. 1. Aerosol properties are listed in Table 4. Target range, $L = 5 \text{ km}$; beam focus = 5 km ; target area = 100 cm^2 ; wind speed, $V_w = 5 \text{ m/sec}$; turbulence strength, $C_n^2 = 10^{-15} \text{ m}^{-2/3}$; pointing jitter angular amplitude = $2 \mu\text{rad}$ (white noise).

P_T . In this regime, the 1.625 μm , and 2.141 μm wavelengths provide slightly greater power on target than 1.045 μm . This is due to the lower aerosol scattering coefficient associated with the longer wavelengths. For $P_T < 1\text{ MW}$, the propagation efficiency is roughly 50% for the three wavelengths considered. For example, $P_T = 1\text{ MW}$ results in $\langle P_{\text{target}} \rangle \sim 0.55\text{ MW}$ for $\lambda = 1.625\mu\text{m}$ and $\lambda = 2.141\mu\text{m}$. However, for $P_T > 1.5\text{ MW}$, thermal blooming becomes important. In this high power regime the optimum wavelength is 1.045 μm due to the lower molecular absorption coefficient in that water vapor window. For $P_T = 3\text{ MW}$, $\langle P_{\text{target}} \rangle \sim 1\text{ MW}$ for 1.045 μm while $\langle P_{\text{target}} \rangle \sim 0.8\text{ MW}$ for 1.625 μm and 2.141 μm . The power on target decreases for larger values of transmitted power not included in the plot.

The effect of thermal blooming on the laser spot size on target is shown in Fig. 6. Figure 6 shows contours of the time averaged intensity in the target plane for three values of transmitted power at $\lambda = 1.625\mu\text{m}$. The time average is performed over the entire dwell time of 1 sec. The laser spot size on target is seen to increase with increasing P_T . For relatively low power, $P_T = 0.5\text{ MW}$, the beam is focused within the 100 cm^2 target area and the loss of power on the target is mainly due to aerosol scattering. When $P_T = 1\text{ MW}$, the laser beam extends slightly beyond the target area. For $P_T = 3\text{ MW}$, the beam cross section is much larger than the target area and exhibits a crescent shape characteristic of thermal blooming in the presence of a wind. In these simulations, aerosol vaporization effects increased the average power on target by $\sim 10\%$ for $P_T \geq 1.5\text{ MW}$.

ii) Desert Environment

The desert aerosol environment is characterized by dry, dust-like aerosols which cannot be vaporized at the laser intensities considered here. These aerosols absorb laser energy, heat the surrounding air and significantly contribute to thermal blooming. The aerosol absorption and scattering coefficients, generated using the MODTRAN4 desert model with a 10 km visibility, are shown in Table 5 for the three wavelengths of interest.

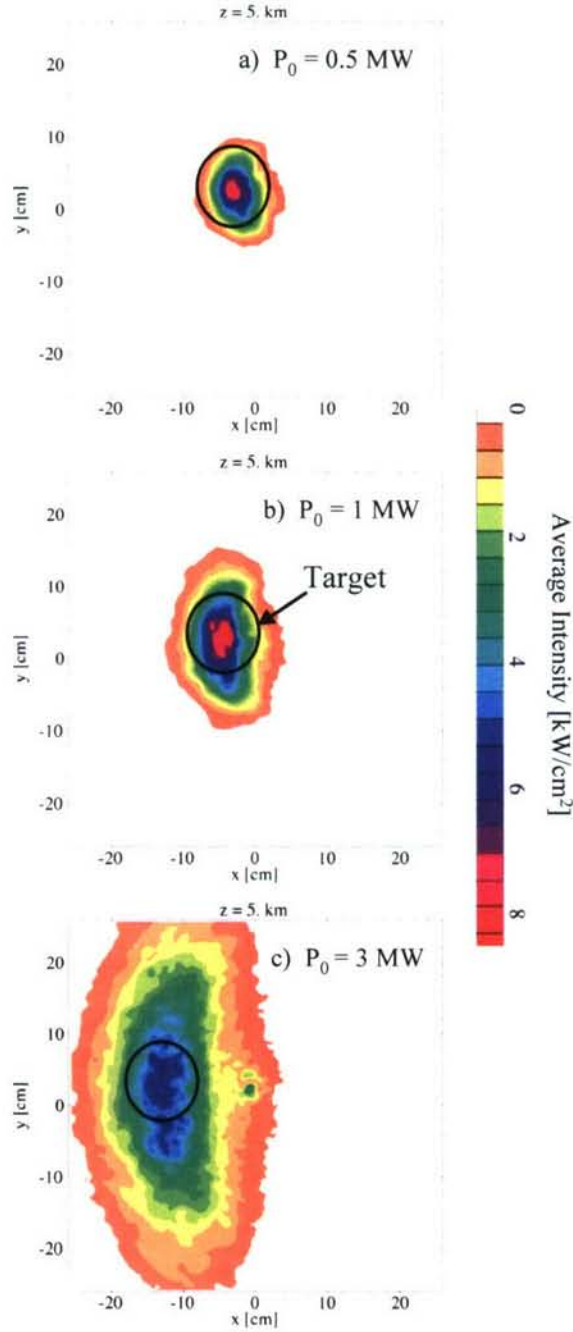


Figure 6: Time-averaged intensity in the target plane for transmitted powers, a) $P_T = 0.5$ MW, b) $P_T = 1$ MW, and c) $P_T = 3$ MW, and $\lambda = 1.625 \mu\text{m}$. Time average is done over 1 sec dwell time. Parameters correspond to those of Fig. 5.

The molecular absorption coefficients are taken to be the same as in the maritime environment.

Figure 7 plots the average power on target versus transmitted power, P_T , for the three wavelengths of interest. The results are qualitatively similar to those of the maritime environment, i.e., the optimum wavelengths are 1.625 μm and 2.141 μm for $P_T < 2$ MW, and 1.045 μm for $P_T > 2$ MW. In a desert environment, $P_T = 1$ MW results in $\langle P_{\text{target}} \rangle \sim 0.5$ MW for 1.625 μm and 2.141 μm wavelengths, and $\langle P_{\text{target}} \rangle \sim 0.35$ MW for 1.045 μm . For $P_T = 3$ MW, $\langle P_{\text{target}} \rangle \sim 1.3$ MW for 1.045 μm , ~ 0.8 MW for 1.625 μm , and ~ 0.7 MW for 2.141 μm wavelengths.

iii) Rural Environment

The rural aerosol environment is taken to be a mixture of 70% water soluble aerosols and 30% dust-like aerosols [27]. The total aerosol absorption and scattering coefficients for the rural environment are shown in Table 6. These coefficients are generated using the MODTRAN4 rural model with a 10 km visibility. At the laser intensity levels considered, the dust-like aerosols are not vaporized while the water soluble aerosols are partially vaporized. In the vaporization calculations, the absorption coefficient of the aerosol droplet is taken to be $\alpha_D = 1.2 \times 10^3 \text{ cm}^{-1}$, $1.0 \times 10^3 \text{ cm}^{-1}$, and $3.5 \times 10^2 \text{ cm}^{-1}$ for the wavelengths $\lambda = 1.045 \text{ }\mu\text{m}$, 1.625 μm , and 2.141 μm , respectively. These values are calculated using the refractive index for water soluble aerosols [27], assuming 80% RH.

Figure 8 plots the average power on target versus transmitted power for the rural environment. Because of the large absorption coefficient of the water soluble and dust aerosols thermal blooming begins to be a limiting process for $P_0 > 0.5$ MW. For the rural environment, 2.141 μm is the optimum wavelength over the entire range $P_T < 0.3$ MW. The optimum power for a wavelength of 2.141 μm is $P_T \sim 1.5$ MW which results in $\langle P_{\text{target}} \rangle \sim 0.6$ MW. For $P_T > 1.5$ MW, the power on target is limited by thermal blooming.

Desert Environment		
λ [μm]	α_A [km^{-1}]	β_A [km^{-1}]
1.045	7×10^{-4}	0.17
1.625	5×10^{-4}	0.097
2.141	6×10^{-4}	0.072

Table 5: Aerosol absorption (α_A) and scattering (β_A) coefficients at wavelengths $\lambda = 1.045, 1.625, 2.141 \mu\text{m}$ for a model desert environment generated using MODTRAN4, 10 km visibility.

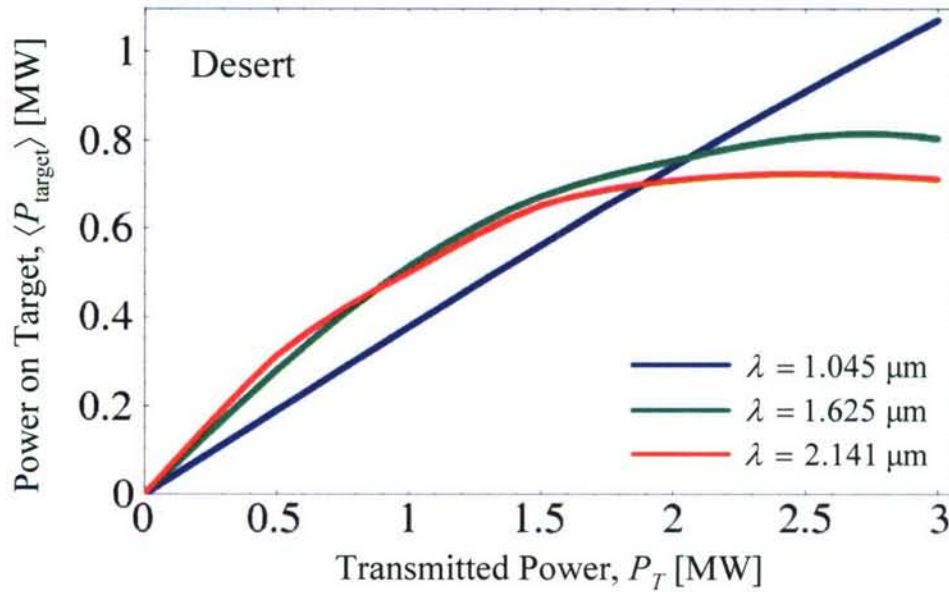


Figure 7: Average power on target, $\langle P_{\text{target}} \rangle$, versus transmitted power, P_T , in a desert environment for the wavelengths $\lambda = 1.045, 1.625, 2.141 \mu\text{m}$. Initial beam profile has $R_0 = 50 \text{ cm}$, $D = 80 \text{ cm}$. Simulation geometry is shown in Fig. 1. Aerosol properties are listed in Table 5. Target range, $L = 5 \text{ km}$; beam focus = 5 km ; target area = 100 cm^2 ; wind speed, $V_w = 5 \text{ m/sec}$; turbulence strength, $C_n^2 = 10^{-15} \text{ m}^{-2/3}$; pointing jitter angular amplitude = $2 \mu\text{rad}$ (white noise).

iv) Urban Environment

The aerosol absorption and scattering coefficients are generated using the MODTRAN4 urban aerosol model with a 10 km visibility. Table 7 lists the calculated scattering and absorption coefficients. The aerosol absorption in an urban environment is the largest of the four environments considered. Urban aerosols are modeled as a mixture of 80% rural aerosols and 20% soot aerosols [27]. Soot aerosols, which cannot be vaporized, represent the dominant contribution to aerosol absorption. Hence they heat the air and cause significant thermal blooming of the laser.

Figure 9 plots the average power on target versus the transmitted power. For the urban environment, 2.141 μm is the optimum wavelength over the entire range

$P_T < 3 \text{ MW}$. The optimum transmitted power for the 2.141 μm wavelength is $P_T \sim 0.3 \text{ MW}$, which results in a power on target of only $\langle P_{\text{target}} \rangle \sim 0.09 \text{ MW}$.

v) Air-to-Ground Propagation in Desert and Urban Environments

Finally, we consider the propagation of a HEL beam from a high altitude fast-moving airborne platform or plane, to a stationary target on the ground. The plane is located at $z = 0$ and the target is at $z = L = 5 \text{ km}$. The laser beam has an effective slew velocity of $V_w = V_0[1 - (z/L)]$, where $V_0 = 100 \text{ m/sec}$ is the plane velocity. The background wind velocity is zero. This configuration produces a stagnation zone near the ground, i.e., target. The turbulence strength, scattering coefficients, and absorption coefficients are assumed to vary with atmospheric density according to, for example, $C_n^2 = C_{n,g}^2 \exp[(z - L)/L_{\text{atm}}]$ where $C_{n,g}^2 = 10^{-15} \text{ m}^{-2/3}$ is the turbulence strength at ground level and $L_{\text{atm}} = 8 \text{ km}$ is the characteristic height scale for the atmospheric density. All other parameters are the same as in the previous examples. The range to the target is assumed to be constant.

Figure 10 plots the average power on target versus the transmitted power for a desert and urban environment. It is seen that in the desert environment the large slew effectively reduces thermal blooming and results in propagation efficiencies of greater than $\eta \approx 60\%$ for the case of the 2.141 μm wavelength laser. In the urban environment,

Rural Environment		
λ [μm]	α_A [km^{-1}]	β_A [km^{-1}]
1.045	0.016	0.15
1.625	0.012	0.076
2.141	0.006	0.053

Table 6: Aerosol absorption (α_A) and scattering (β_A) coefficients at wavelengths $\lambda = 1.045, 1.625, 2.141 \mu\text{m}$ for a model rural environment generated using MODTRAN4, 10 km visibility.

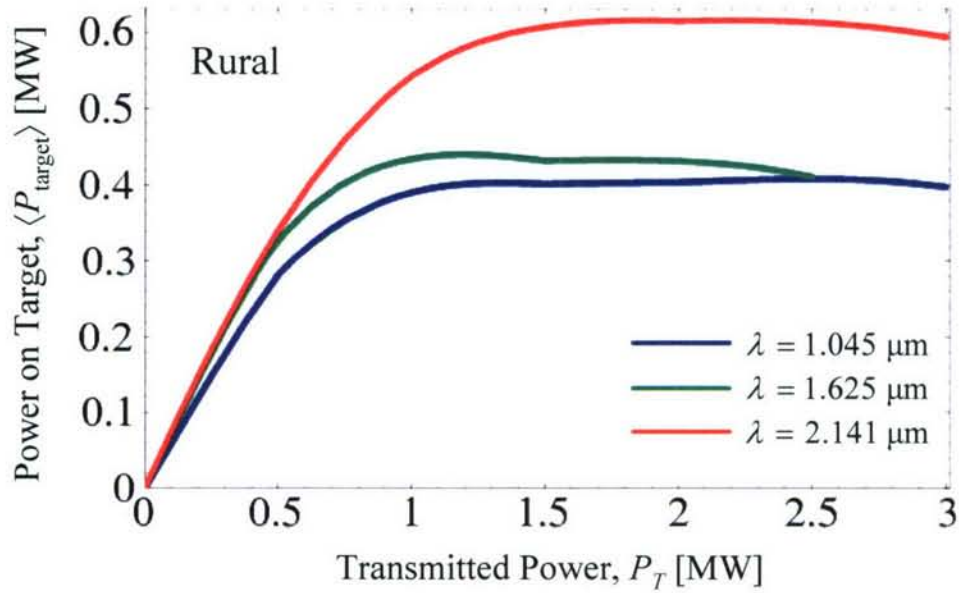


Figure 8: Average power on target, $\langle P_{\text{target}} \rangle$, versus transmitted power, P_T , in a rural environment for the wavelengths $\lambda = 1.045, 1.625, 2.141 \mu\text{m}$. Initial beam profile has $R_0 = 50 \text{ cm}$, $D = 80 \text{ cm}$. Simulation geometry is shown in Fig. 1. Aerosol properties are listed in Table 6. Target range, $L = 5 \text{ km}$; beam focus $= 5 \text{ km}$; target area $= 100 \text{ cm}^2$; wind speed, $V_w = 5 \text{ m/sec}$; turbulence strength, $C_n^2 = 10^{-15} \text{ m}^{-2/3}$; pointing jitter angular amplitude $= 2 \mu\text{rad}$ (white noise).

Urban Environment		
λ [μm]	α_A [km^{-1}]	β_A [km^{-1}]
1.045	0.05	0.13
1.625	0.036	0.065
2.141	0.028	0.044

Table 7: Aerosol absorption (α_A) and scattering (β_A) coefficients at wavelengths $\lambda = 1.045, 1.625, 2.141 \mu\text{m}$ for a model urban environment generated using MODTRAN4, 10 km visibility.

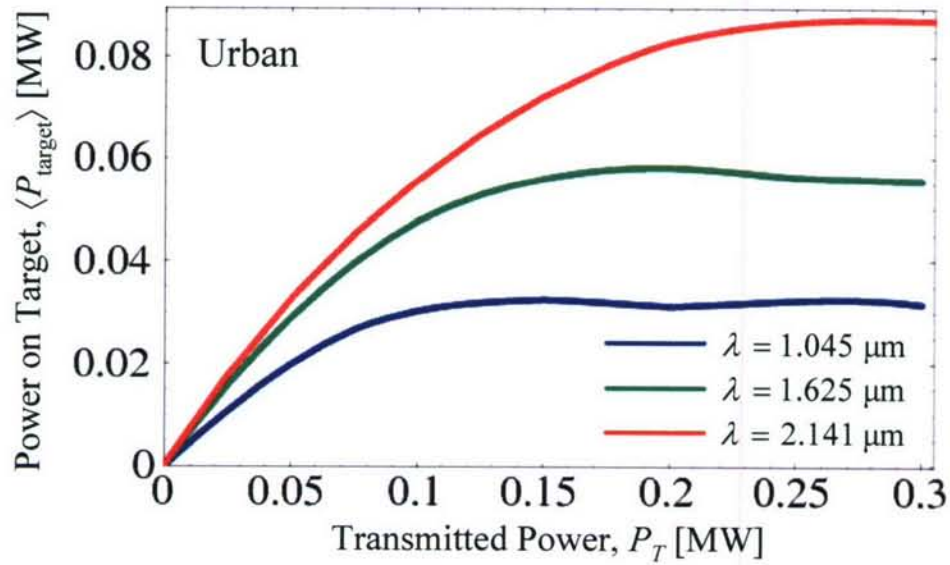


Figure 9: Average power on target, $\langle P_{\text{target}} \rangle$, versus transmitted power, P_T , in an urban environment for the wavelengths $\lambda = 1.045, 1.625, 2.141 \mu\text{m}$. Initial beam profile has $R_0 = 50 \text{ cm}$, $D = 80 \text{ cm}$. Simulation geometry is shown in Fig. 1. Aerosol properties are listed in Table 7. Target range, $L = 5 \text{ km}$; beam focus = 5 km ; target area = 100 cm^2 ; wind speed, $V_w = 5 \text{ m/sec}$; turbulence strength, $C_n^2 = 10^{-15} \text{ m}^{-2/3}$; pointing jitter angular amplitude = $2 \mu\text{rad}$ (white noise).

thermal blooming is still a limiting factor due to the large absorption of soot aerosols. However, the propagation efficiency in this vertical propagation example is much greater than for the urban horizontal propagation example of Fig. 9. For the optimum wavelength of $2.141\mu\text{m}$, the propagation efficiency at $P_T = 1 \text{ MW}$ is $\eta \approx 45\%$.

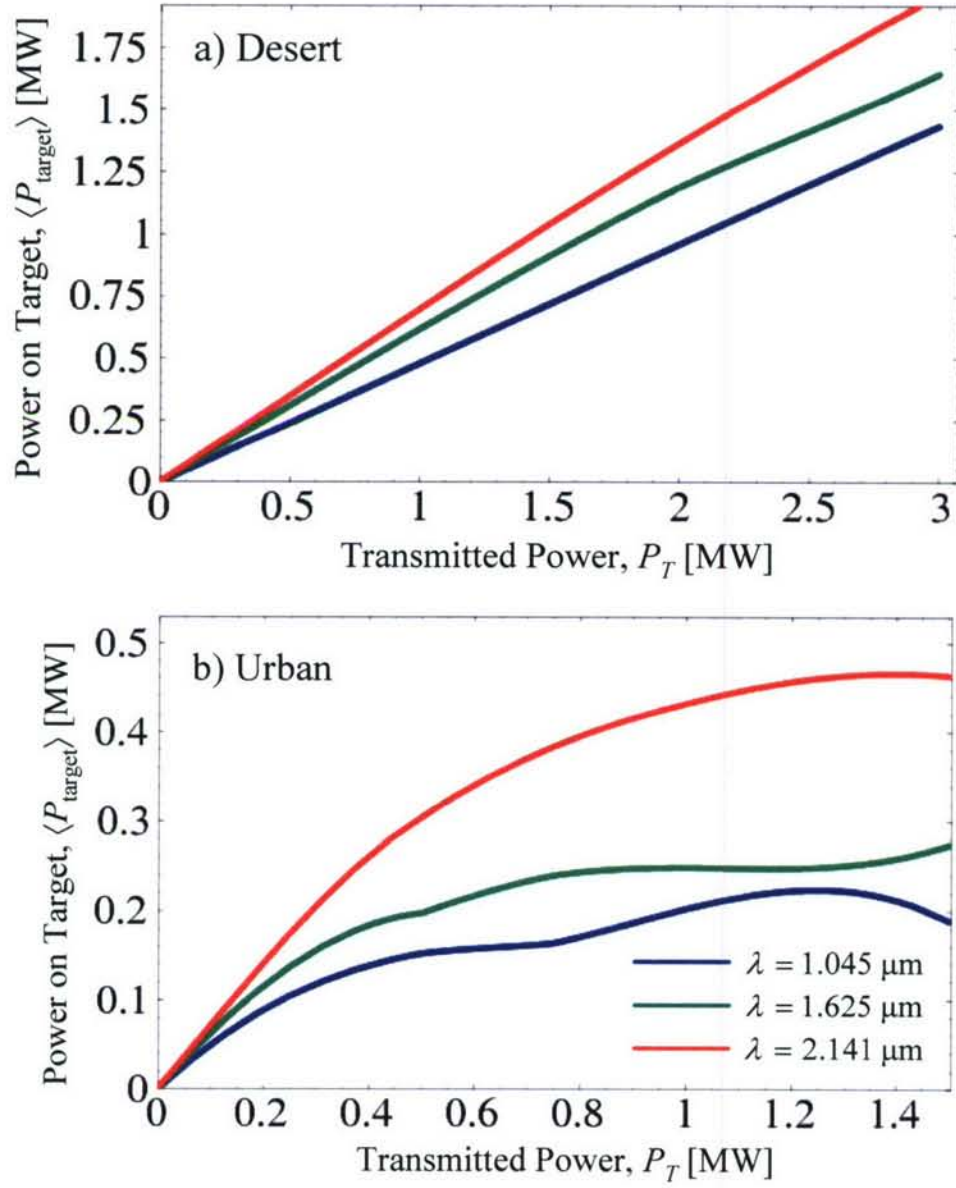


Figure 10: Average power on target, $\langle P_{\text{target}} \rangle$, versus transmitted power, P_T , in a a) desert environment and b) urban environment for the wavelengths $\lambda = 1.045$, 1.625 , and $2.141 \mu\text{m}$ for vertical air-to-ground propagation. Initial beam profile has $R_0 = 50 \text{ cm}$, $D = 80 \text{ cm}$. Simulation geometry is shown in Fig. 1. Aerosol properties are listed in Tables 5 and 7. Target range, $L = 5 \text{ km}$; beam focus = 5 km ; target area = 100 cm^2 ; wind speed, $V_w = V_0[1 - (z/L)]$, $V_w = 100 \text{ m/sec}$; turbulence strength, $C_n^2 = C_{n,g}^2 \exp[(z-L)/L_{\text{atm}}]$, $C_{n,g}^2 = 10^{-15} \text{ m}^{-2/3}$, $L_{\text{atm}} = 8 \text{ km}$; pointing jitter angular amplitude = $2 \mu\text{rad}$ (white noise).

VII. HEL Propagation Through a Stagnation Zone

High energy laser beams propagating through the atmosphere can be severely defocused or deflected by thermal blooming [1]. The thermal blooming process is driven by a small fraction of the laser energy that is absorbed by the molecular and aerosol constituents of air [10,28]. The absorbed energy locally heats the air and leads to a decrease in the air density which modifies the refractive index. The refractive index variation leads to a defocusing or deflection of the laser beam. In the presence of a transverse wind, the region of heated air is convected out of the beam path and a steady-state situation is realized [1]. In general, however, the intensity of a beam undergoing thermal blooming is a function of both time and spatial position, particularly in a stagnation zone, where the effective wind velocity is zero.

Stagnation zones are particularly detrimental to HEL propagation since, without an effective clearing mechanism for the heated air, the strength of the thermal lens grows in time. In this situation, the defocusing process is eventually limited by thermal conduction or buoyancy. However, by the time these processes become effective, the beam may have already been severely degraded.

Thermal blooming in the presence of a stagnation zone was experimentally observed in a laboratory experiment using a 10W, CO_2 laser passed through an absorption cell containing CO_2 gas. The cell was pivoted to simulate a wind profile containing a stagnation zone. This experiment was also modeled using a code that solved time-dependent thermal blooming equations in the isobaric regime [16].

In this Section we examine the effect of a stagnation zone on a HEL beam focused onto a remote target in a maritime atmosphere. We first analyze the effect of a stagnation zone on the propagation of a focused beam and calculate an approximate expression for the relative intensity (Strehl ratio) on target as a function of focusing geometry and stagnation zone position. We then utilize the HELCAP code [28] to examine the propagation of a megawatt-class HEL beam through a maritime atmosphere which contains a stationary stagnation zone along the laser path. The laser target configuration used in these simulations is shown in Fig. 1. Our simulation model includes time-dependent thermal blooming as well as aerosol and molecular absorption [10,28], turbulence [2], aerosol and molecular scattering [3], and aerosol heating and vaporization

[4-6]. We use the simulations to calculate the laser power delivered to a remote target for different wind profiles which place the stagnation zone at different locations along the laser propagation path.

i) Analysis

The effect of a stagnation zone on HEL propagation in the atmosphere is highly dependent on laser and atmospheric parameters as well as on the propagation geometry. In general, the problem requires a numerical simulation to determine the amount of power reaching a remote target. Before presenting results of full-scale propagation simulations, however, it is useful to analyze the following simpler problem.

Consider a focused laser beam of wavelength, λ , propagating from $z = 0$ to a remote target at a range $z = L$, where z denotes the propagation coordinate. The focal length of the laser beam, L_f , is such that $L_f \geq L$. The wind speed, $V(z)$ is only a function of z and has a stagnation point defined by $V(z_0) = 0$, where $0 < z_0 < L$. The atmosphere is characterized by an absorption coefficient, α , and a scattering coefficient, β . Turbulence is neglected in this analysis. This configuration allows an approximate expression for the Strehl ratio (relative intensity) at the target to be calculated analytically as a function of both the location of the absorbing region and the laser focal length.

The propagation of the laser beam is described by the paraxial wave equation

$$\frac{\partial A}{\partial z} = \left(\frac{i}{2k_0} \nabla_{\perp}^2 + i \frac{\omega_0}{c} \delta n_{TB} - \frac{\beta}{2} \right) A, \quad (21)$$

where the laser electric field is $\mathbf{E} = A \exp[i(\omega_0 z/c - \omega_0 t)] \hat{\mathbf{e}}_x / 2 + c.c.$, $\omega_0 = 2\pi c/\lambda$, $\hat{\mathbf{e}}_x$ is a unit polarization vector in the x direction, $k_0 = n_0 \omega_0 / c$, n_0 is the ambient refractive index, ∇_{\perp} is the gradient operator in the transverse direction, c is the speed of light in vacuum, δn_{TB} is the change in refractive index induced by the laser, and $c.c.$ denotes the complex conjugate. In the absence of a transverse wind or slew, there is axial symmetry about the z -axis and all spatially varying quantities are functions of (r, z, t) only, where r is the radial coordinate and t is time. Writing $A(r, z, t) = B(r, z, t) \exp[i\theta(r, z, t)]$, where B , θ , and δn_{TB} are assumed to be real, leads

to the following equations for the laser intensity I ($\sim B^2$) and the transverse wavenumber $\mathbf{k}_\perp = \nabla_\perp \theta$:

$$\frac{\partial I}{\partial z} = -\frac{1}{k_o} \nabla_\perp \cdot (\mathbf{k}_\perp I) - \beta I, \quad (22)$$

$$\frac{\partial \mathbf{k}_\perp}{\partial z} = \frac{1}{8k_o} \nabla_\perp \left\{ \frac{1}{I^2} (2I \nabla_\perp^2 I - (\nabla_\perp I)^2) \right\} - \frac{1}{k_o} \mathbf{k}_\perp \cdot \nabla_\perp \mathbf{k}_\perp + \frac{\omega_o}{c} \nabla_\perp \delta n_{TB}. \quad (23)$$

On the right side of Eq. (23), the first term is of order $\sim \lambda / R^3$ where R is the laser spot size. The second term is of order $\sim R / (L_f^2 \lambda)$ for a focused beam and the third term is of order $\sim \delta n_{TB} / (\lambda R)$. We consider parameters such that $R \sim 50$ cm, $\lambda \sim 1$ μ m, and $L_f \sim 5$ km. In this parameter regime, the second term is much larger than the first term. The third term is much larger than the second term for $\delta n_{TB} > 10^{-8}$, which is typically encountered within a stagnation zone. Hence, for the parameter regime of interest, we neglect the first and second terms on the right side of Eq. (23) and integrate to solve for \mathbf{k}_\perp , i.e.,

$$\mathbf{k}_\perp(r, z, t) \approx \mathbf{k}_{\perp 0}(r) + \frac{\omega_o}{c} \int_0^z \nabla_\perp \delta n_{TB}(r, z', t) dz', \quad (24)$$

where $\mathbf{k}_{\perp 0}(r)$ is the initial transverse wavenumber at $z = 0$. Equation (24) represents \mathbf{k}_\perp in the geometric optics limit.

Equation (22) can be integrated to yield

$$I(r, z, t) = I(r, 0, t) e^{-\beta z} \exp \left\{ -\frac{c}{\omega_0} \int_0^z \frac{1}{I(r, z', t)} \nabla_\perp \cdot [\mathbf{k}_\perp(r, z', t) I(r, z', t)] dz' \right\}, \quad (25)$$

which is an integral equation for $I(r, z, t)$ that can be solved approximately by replacing $I(r, z, t)$ in the right side by $I_0(r, z)$, i.e., the unperturbed intensity for a homogeneous medium ($\delta n_{TB} = 0$). The unperturbed intensity satisfies

$$I_0(r, z) = I(r, 0) e^{-\beta z} \exp \left\{ -\frac{c}{\omega_0} \int_0^z \frac{1}{I_0(r, z')} \nabla_\perp \cdot [\mathbf{k}_{\perp 0}(r) I_0(r, z')] dz' \right\}. \quad (26)$$

Substituting Eq. (24) into Eq. (25) yields the relative intensity [29]

$$\frac{I(r, z, t)}{I_0(r, z)} = \exp \left\{ - \int_0^z \frac{dz'}{I_0(r, z')} \nabla_{\perp} \cdot \left[I_0(r, z') \int_0^{z'} dz'' \nabla_{\perp} \delta n_{TB}(r, z'', t) \right] \right\}. \quad (27)$$

The refractive index change due to thermal blooming is given by $\delta n_{TB} = (n_0 - 1) \delta \rho / \rho_0$, where ρ_0 is the mass density, and $\delta \rho$ is the perturbed mass density. In the isobaric regime, the mass density change is given by [1,28]

$$C_p T_0 \left(\frac{\partial}{\partial t} + \mathbf{V} \cdot \nabla - \frac{\kappa}{C_p \rho_0} \nabla^2 \right) \delta \rho = -\alpha_{TB}(\mathbf{r}, t) I, \quad (28)$$

where κ is the thermal conductivity, \mathbf{V} is the effective wind velocity, C_p is the specific heat at constant pressure, T_0 is the ambient temperature, and I is the time-averaged laser intensity. In general, the absorption coefficient, α_{TB} , contains both aerosol and molecular contributions and can be time dependent. For the simplified analysis of this Section, however, we take it to be constant in time. The isobaric approximation is valid for times greater than the hydrodynamic time R/C_s , where C_s is the acoustic speed. We consider time scales less than the thermal conduction time, $C_p \rho_0 R^2 / \kappa$, and neglect the thermal conduction term in Eq. (28).

For the purpose of obtaining an approximate closed form expression for Eq. (27), we solve Eq. (28) approximately by writing the operator $\mathbf{V} \cdot \nabla \approx 1/\tau_c(z)$ where $\tau_c(z) = R(z)/|V(z)|$ is the clearing time. Using this approximation, we can integrate Eq. (28) to obtain

$$\delta n_{TB}(r, z, t) \approx -\gamma_{TB} \alpha I_0(r, z) \tau_c(z) \{1 - \exp[-t/\tau_c(z)]\}, \quad (29)$$

where $\gamma_{TB} \equiv (n_0 - 1)/(C_p T_0 \rho_0)$.

The unperturbed intensity is taken to have a Gaussian transverse profile

$$I_0(r, z) = \frac{I_{00} R_0^2}{R^2(z)} \exp \left[-\frac{r^2}{R^2(z)} \right] e^{-\beta z}, \quad (30)$$

where I_{00} denotes the intensity on axis at $z = 0$. The spot size R is a function of z and the initial spot size is denoted by $R_0 \equiv R(z = 0)$. Substituting Eqs. (29) and (30) into Eq. (27), results in an expression for the on-axis Strehl ratio at $z = L$, i.e.,

$$\frac{I(r = 0, L, t)}{I_0(r = 0, L)} = \exp \left[-8I_{00} R_0^2 \gamma_{TB} \alpha \int_0^L dz' \int_0^{z'} dz'' G(z'', t) \right], \quad (31)$$

where $G(z, t) = \tau_c(z) [1 - \exp(-t/\tau_c(z))] \exp(-\beta z) / R^4(z)$. To obtain an approximate analytic expression for the right side of Eq. (31), we note that for a weakly focused beam, the integrand G is sharply peaked and grows linearly with time in the vicinity of the stagnation zone, i.e., $G(z_0, t) = t \exp(-\beta z_0) / R^4(z_0)$. Hence, we can approximate the integration over z'' in Eq. (31) by

$$\int_0^{z'} dz'' G(z'', t) \approx G(z_0, t) \Delta z \Theta(z' - z_0), \quad (32)$$

where Δz is the characteristic width of the stagnation region and Θ is the Heaviside step function.

Using Eqs. (32) in Eq. (31) results in

$$\frac{I(r = 0, L, t)}{I_0(r = 0, L)} \approx \exp \left[-\frac{8\gamma_{TB} \alpha I_{00} L^2 t}{R_0^2} \left(\frac{\Delta z}{L} \right) \left(1 - \frac{z_0}{L} \right) \frac{R_0^4 \exp(-\beta z_0)}{R^4(z_0)} \right] \quad (33)$$

The width of the stagnation region, Δz , is in general a function of time and also the spatial variation of the wind profile. We can define the stagnation zone as the region where the condition $t / \tau_c(z) \ll 1$ is satisfied. In this case, the width of the stagnation zone can be defined according to $t / \tau_c(z_0 + \Delta z) = 1$.

We now consider specific analytic expressions for the wind profile $V(z)$ and laser spot size $R(z)$. For a slewed laser beam, the wind profile can be written as

$$V(z) = V_{wind} (1 - z / z_0), \quad (34)$$

where V_{wind} is the ambient wind velocity, and the laser slew rate, $\dot{\theta}$ is related to z_0 according to $\dot{\theta} = V_{wind} / z_0$. Note that for this model, a stagnation zone at the transmitter

($z = 0$) implies an infinite slew rate. Assuming that the laser spot size does not vary appreciably within the stagnation zone,

$$\Delta z \approx z_0 R(z_0) / (V_{wind} t) \quad (35)$$

for the wind profile of Eq. (34).

For the linearly varying wind profile described above, Eq. (33) can be written as

$$\frac{I(r=0, L, t)}{I_0(r=0, L)} \approx \exp \left[-\frac{8\gamma_{TB} \alpha I_{00} L^2}{R_0 V_{wind}} f(z_0) \right], \quad (36)$$

where

$$f(z_0) = \left(\frac{z_0}{L} \right) \left(1 - \frac{z_0}{L} \right) \frac{R_0^3 \exp(-\beta z_0)}{R^3(z_0)} \quad (37)$$

describes how the location of the stagnation zone affects the relative intensity on target. The larger the value of $f(z_0)$, the lower the intensity on the target.

We can derive an approximate functional form for $R(z)$ to be used in Eq. (37). Substituting Eq. (30) into Eq. (26), the laser spot size can be shown to satisfy $R(z) = R_0[1 - z(1 - \eta)/L]$ for $z \ll L_f$, where the parameter $\eta \equiv R(L)/R_0$, i.e., the ratio of the spot size on target to the initial spot size. In terms of the focal length, $\eta = 1 - (L/L_f)$. Phenomenologically, η can also parameterize focusing limitations due to beam quality or atmospheric turbulence.

Figure 11 plots the distortion function f versus z_0 for various values of η . We assume a normalized scattering coefficient of $\beta L = 0.25$. For a beam that is focused near the target plane, the distortion at the target plane is largest when the stagnation zone is close to the target. In contrast, when the beam is collimated ($\eta \sim 1$), the distortion at the target plane is greater when the stagnation zone is closer to the laser source. Note that the case $z_0 = 0$, which corresponds to an infinite slew rate given the assumed wind profile of our model, is not physically realizable.

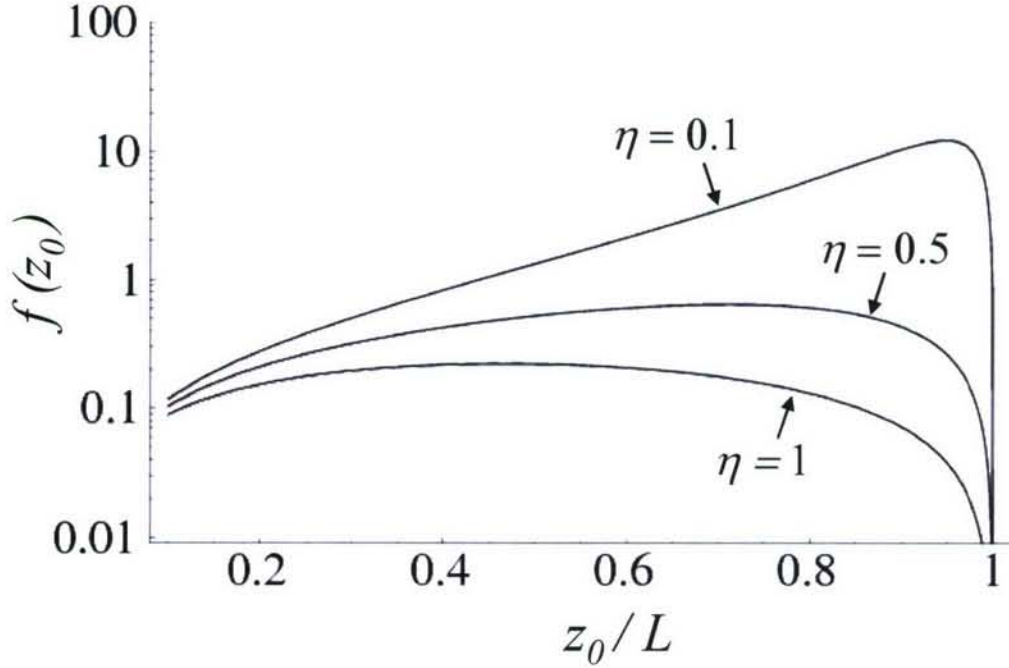


Figure 11: Distortion function f as defined by Eq. (17) plotted versus distance to stagnation zone z_0 for various values of the focusing parameter $\eta = R(L)/R_0$ where $R(L)$ is the unperturbed laser spot size at the target plane ($z = L$), R_0 is the initial spot size at $z = 0$, and $\beta L = 0.25$.

ii) Numerical Simulation

For the numerical simulations presented here, we use the HELCAP code and consider a slewed HEL beam focused at a range of $L = 5$ km in the presence of a uniform transverse wind. The z -axis defines the direction of propagation and the wind and slew velocities are taken to be along the y -axis. The simulation geometry is shown in Fig. 1.

The high energy laser beam has an initial field profile given by

$A = A_0 f(r) g(t) \exp(-r^2/R_0^2)$, where $f(r) = \exp[-(2r/D)^\ell]$, $\ell = 20$, limits the transverse extent of the beam to the aperture diameter, D . The function $g(t)$ is the initial temporal profile of the beam which contains a pointing jitter characterized by an angular spread of $2 \mu\text{rad}$ and a white noise temporal spectrum. The transmitted power at the source is denoted by P_T .

The laser is propagated through a maritime environment in which the aerosol distribution is modeled using the Advanced Navy Aerosol Model (ANAM) [12] and the molecular absorption coefficient is calculated using MODTRAN4 [19]. The details of the atmospheric model and the parameters used to characterize a maritime environment are discussed in previous chapters of this report. The ambient absorption and scattering coefficients for propagation at $\lambda = 2.141 \mu\text{m}$ are $\alpha_{TB} = 6 \times 10^{-3} \text{ km}^{-1}$ and $\beta = 0.05 \text{ km}^{-1}$, respectively. In the simulations these quantities vary in space and time due to aerosol vaporization.

The effective wind speed along the propagation path is $V(z) = V_{\text{wind}} - \dot{\theta} z$, where z is the distance from the laser source, V_{wind} is the ambient wind speed, and $\dot{\theta}$ is the laser beam slew rate. For positive $\dot{\theta}$, i.e., slewing in the direction of the wind, a stagnation zone is created at location $z_0 = V_{\text{wind}} / \dot{\theta}$. In what follows, we investigate the effect of this stagnation zone on the propagation of a HEL beam for various slew rates which change the distance from the transmitter to the stagnation zone.

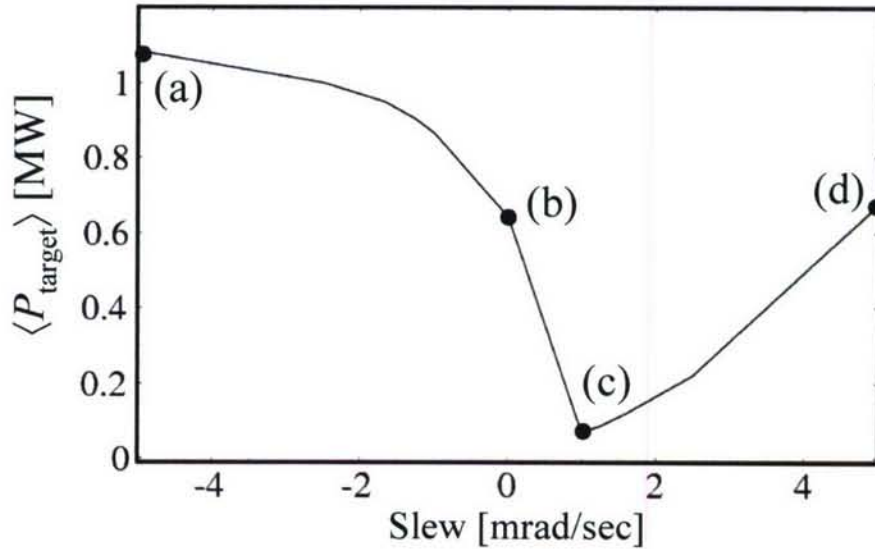


Figure 12: Average power on target, $\langle P_{\text{target}} \rangle$, versus slew rate for $\lambda = 2.141 \mu\text{m}$, $P_T = 1.5 \text{ MW}$, $V_{\text{wind}} = 5 \text{ m/sec}$, $\tau_{\text{dwell}} = 1 \text{ sec}$, and $L = 5 \text{ km}$. Points (a), (b), (c), and (d) are labeled to correspond with fluence distributions shown in Fig. 4.

iii) Results

We consider a laser of wavelength $\lambda = 2.141\mu\text{m}$ and power $P_T = 1.5\text{ MW}$ propagating through a maritime atmosphere with $V_{wind} = 5\text{ m/sec}$. The power delivered to a target of circular area 100 cm^2 at a range of 5 km is used as a figure of merit. In the simulations that follow, the target is always located such that the peak laser fluence at 5 km range is at the center of the target. The average power reaching the target is defined by

$$\langle P_{\text{target}} \rangle = \frac{1}{\tau_{\text{dwell}}} \int_0^{\tau_{\text{dwell}}} d\tau \int dx dy I(x, y, z = L, \tau), \quad (38)$$

where the dwell time $\tau_{\text{dwell}} = 1\text{ sec}$, and $dx dy$ is the differential cross section which is integrated over the target area. The total laser energy reaching the target is

$$E_{\text{target}} = \langle P_{\text{target}} \rangle \tau_{\text{dwell}}.$$

Figure 12 plots $\langle P_{\text{target}} \rangle$ versus slew rate, $\dot{\theta}$, for the propagation configuration of Fig. 1. A negative slew denotes that the slew direction is opposite to the wind direction. In this case, there is no stagnation zone between the laser and the target. A positive slew denotes slew in the direction of the wind. In this case, it is possible to have a stagnation zone somewhere along the propagation path. For example, a slew rate of 1 mrad/sec places the stagnation zone at the target, while a slew rate of 5 mrad/sec places the stagnation zone 1 km from the laser source. Figure 12 shows that in the absence of slew (i.e., uniform wind), the power on target is $\langle P_{\text{target}} \rangle \approx 0.7\text{ MW}$ and the propagation efficiency is $\sim 50\%$. $\langle P_{\text{target}} \rangle$ increases relative to this value when the slew is opposite to the wind direction because the effectively larger wind speed along the entire propagation path mitigates thermal blooming. For a slew rate $\dot{\theta} = -5\text{ mrad/sec}$, for example, $\langle P_{\text{target}} \rangle \approx 1.1\text{ MW}$, which corresponds to a propagation efficiency of $> 70\%$.

When the slew is increased in the direction of the wind, the power on target decreases sharply for $\dot{\theta} < 1\text{ mrad/sec}$ and reaches a minimum when $\dot{\theta} = 1\text{ mrad/sec}$, i.e., when the stagnation zone is at the target. At this minimum, $\langle P_{\text{target}} \rangle \approx 0.07\text{ MW}$,

which corresponds to a propagation efficiency of $< 5\%$. Increasing the slew rate further brings the stagnation zone closer to the laser source, where the intensity is lower, and increases the effective wind velocity near the target. The result is that the power on target increases with slew rate. For a slew rate of $\dot{\theta} = 5 \text{ mrad/sec}$, $\langle P_{\text{target}} \rangle \approx 0.7 \text{ MW}$. These results are consistent with the calculation in Sec. II, i.e., for a beam focused onto the target plane, a stagnation zone close to the target will result in the largest beam distortion.

Figure 13 plots the laser fluence on target calculated over a 1 sec dwell time. Panel labels, (a), (b), (c), and (d) correspond to the different slew rates indicated in Fig. 12. Panel (a) corresponds to a slew rate $\dot{\theta} = -5 \text{ mrad/sec}$, which gives the maximum power on target over the range of slew rates considered. The beam is well-focused and exhibits practically no thermal blooming effects. Panel (b) shows the beam profile when the slew rate is zero, i.e., a uniform wind profile. In this case the beam fluence profile shows the characteristic crescent shape associated with thermal blooming with the centroid of the beam deflected opposite to the direction of the wind. Panel (c) shows the beam profile on target for the case when the stagnation zone is at the target. The beam is severely defocused as a result of thermal blooming. The peak in fluence near $(x = 0, y = 0)$ is due to the leading edge of the beam ($t < 20 \text{ msec}$), which is not affected by the time dependent thermal blooming process. Panel (d) shows the beam profile when the stagnation zone is 1 km from the target. In this case, the effective wind velocity near the target is in the opposite direction relative to that of panel (b). The value of $\langle P_{\text{target}} \rangle$ is similar to that of panel (b) but with the beam deflected in the opposite direction.

Figure 14 shows the time dependence of the beam intensity at the target. Figure 13a corresponds to a slew rate of $\dot{\theta} = -5 \text{ mrad/sec}$, when the power on target is maximum. In this case the beam is well-focused over the entire dwell time. The transverse profile is mainly affected by turbulence and pointing jitter. Figure 13b corresponds to a slew rate of $\dot{\theta} = 1 \text{ mrad/sec}$, which results in the minimum power on target. For this case, it is seen that severe defocusing occurs for times $> 20 \text{ msec}$, while the first $\sim 10 \text{ msec}$ of the beam is relatively unaffected by thermal blooming.

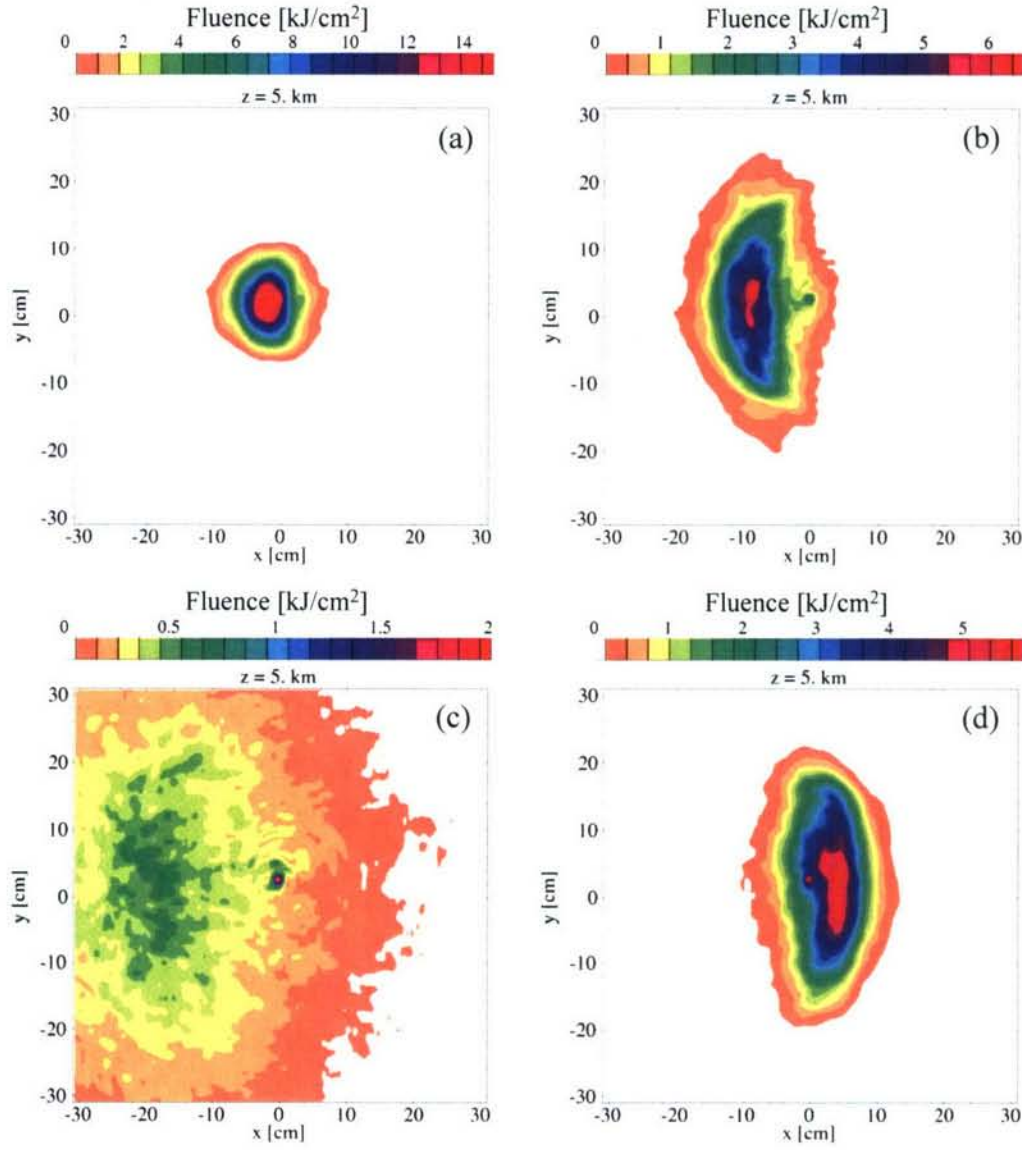


Figure 13: Laser fluence profiles at the target range for slew rates (a) $\dot{\theta} = -5$ mrad/sec , (b) $\dot{\theta} = 0$, (c) $\dot{\theta} = 1$ mrad/sec , and (d) $\dot{\theta} = 5$ mrad/sec . Parameters are the same as those of Fig. 11. Fluence is calculated over a 1 sec dwell time.

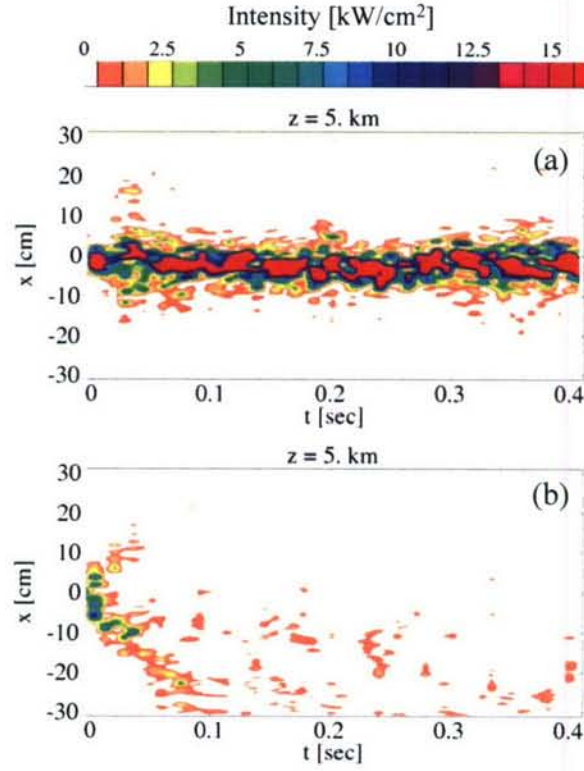


Figure 14: Laser intensity in the $y=0$ plane versus transverse coordinate, x , and time, t , for slew rates (a) $\dot{\theta} = -5$ mrad/sec and (b) $\dot{\theta} = 1$ mrad/sec. Parameters correspond to those of Fig. 11.

VIII. Conclusions

In this study we have analyzed the physical processes that affect the propagation of high energy laser (HEL) beams and employed HELCAP, a fully three-dimensional, time-dependent numerical simulation code, to determine the optimum laser wavelength and power for HEL propagation in maritime, desert, rural, and urban environments. The aerosol absorption and scattering coefficients which characterize these environments were generated using the ANAM and MODTRAN aerosol models.

The theoretical model and numerical simulations contain several interrelated physical processes which affect HEL propagation. These include: i) aerosol and

molecular scattering ii) aerosol heating and vaporization iii) thermal blooming due to both aerosol and molecular absorption iv) atmospheric turbulence and v) laser beam quality. HELCAP is unique in that it contains all of these physical processes in a fully time-dependent and self-consistent manner.

Using HELCAP, we calculated the average power, $\langle P_{\text{target}} \rangle$, delivered to a 100 cm^2 cross sectional area target at a range of 5 km over a 1 second dwell time as a function of transmitted power, P_T , and wavelength. We considered three laser wavelengths corresponding to molecular (water vapor) transmission windows, $1.045 \mu\text{m}$, $1.625 \mu\text{m}$ and $2.141 \mu\text{m}$, and transmitted powers P_T up to 3 MW. We note that in addition to the power propagated to the target, $\langle P_{\text{target}} \rangle$, the absorption efficiency of the target should be considered in evaluating HEL lethality. Target absorption efficiency is relatively insensitive to wavelength in the range considered.

We find that aerosols are of particular importance because they result in laser scattering, absorption, and enhanced thermal blooming. In the water vapor transmission windows, the total absorption coefficient driving thermal blooming can be due mainly to aerosols and not to water vapor. In certain environments and for sufficiently high laser power, scattering and absorption by aerosols can be reduced by vaporization. Aerosols that consist of dust, soot, etc., cannot be vaporized and can significantly enhance thermal blooming. We note that moderate values of the laser beam quality factor M^2 , i.e., values less than 4, have little effect on the propagation of HELs compared to other effects such as, molecular/aerosol thermal blooming and turbulence.

Our results show that the average power on target is strongly dependent on the atmospheric environment as discussed in the Summary. When the propagating efficiency is not a particularly sensitive function of wavelength, as in the maritime and desert environments for $P_T < 1.5 \text{ MW}$, other issues such as laser availability and/or eye safe wavelengths, may become important considerations in determining the optimum wavelength and power. In this study we have reported only on wavelengths in the water vapor transmission windows, $\lambda = 1.045, 1.625, \text{ and } 2.141 \mu\text{m}$. Other laser wavelengths, such as those particular to solid state and chemical lasers, have also been considered. In

general, it is found that at high laser powers, for which thermal blooming is a factor, operating in the water vapor window results in higher propagating efficiencies. We find that propagation efficiencies approaching 60% can be achieved in the absence of stagnation zones.

Experiments are presently underway at the Naval Research Laboratory to study and characterize aerosol-induced thermal blooming and scattering of HEL beams. In these experiments a ~ 1 kW, CW, $\sim 1\mu\text{m}$ fiber laser will interact with both water based and dust like aerosols. Earlier experiments performed at United Aircraft Research Laboratories using a low power 15W, $10.6\mu\text{m}$ laser beam demonstrated enhanced thermal blooming in the presence of carbon aerosols [7].

Stagnation zones can significantly degrade the propagation efficiency of a high energy laser (HEL) through the atmosphere. We have analyzed the propagation of a focused HEL beam through a model atmosphere containing a stagnation zone. Our analysis shows that the amount of laser degradation caused by a stagnation zone is highly dependent on the focusing geometry of the laser beam and the location of the stagnation zone along the propagation path. For a collimated laser beam, a stagnation zone near the transmitter causes the largest distortion of the laser beam on the target. For a laser that is focused onto the target, a stagnation zone near the target causes the largest laser distortion and the fastest decrease in laser intensity. This finding is in agreement with the experimental results of Ref. [16].

We used the HELCAP to model the propagation of a megawatt-class HEL beam through a realistic maritime atmosphere containing a stationary stagnation zone. The HEL beam is focused onto a remote target. The stagnation zone is created by slewing the HEL beam in the direction of the wind and location of the stagnation zone is varied by changing the slew rate. Consistent with our analysis, the simulations show that the power on target is minimized when the slew rate is such that the stagnation zone is located near the target plane. In this case, propagation efficiency can be reduced by an order of magnitude relative to an unslewed beam.

Acknowledgments

The authors thank A. Ting, J. Albertine, J. Reid, S. Doss-Hammel and Q. Saulter for many useful discussions. This work was sponsored by the Joint Technology Office and the Office of Naval Research.

References

- [1] Smith, D.C., "High-Power Laser Propagation - Thermal Blooming," *Proc. IEEE* **65**, 1679 (1977)
- [2] The Infrared and Electro-Optical Systems Handbook, vol. 2, edited by F.G. Smith, Environmental Research Institute of Michigan, Ann Arbor, MI, and SPIE Optical Engineering Press, Bellingham, WA (1993).
- [3] Measures, R.M., "Laser Remote Sensing, Fundamentals and Applications," Krieger Publishing, Malabar, FL (1992)
- [4] Williams, F. A, *Int. J. Heat Mass Transfer*. **8**, 575 (1965).
- [5] Caledonia, G.E. and J.D. Teare, *J. Heat Transfer* **99**, 281 (1977).
- [6] Armstrong, R.L., *Appl. Optics* **23**, 148 (1984); Armstrong, R.L., *J. Appl. Phys.* **56**, 2142 (1984); Armstrong, R.L., S.A.W. Gerstl and A. Zardecki, *J. Opt. Soc. Am. A* **2**, 1739 (1985).
- [7] Davies, S.C. and J.R. Brock, *App. Optics* **26**, 786 (1987)
- [8] Hänel, G., *Beiträge zur Physik der Atmosphäre* **44**, 137 (1971)
- [9] Reid, J.S., D.L. Westphal, R.M. Paulus, S. Tsay and A. van Eijk, "Preliminary Evaluation of the Impacts of Aerosol Particles on Laser Performance in the Coastal Marine Boundary Layer," Naval Research Laboratory, Monterey, CA 93943-5502, NRL/MR/7534—04-8803, Jun. 2004.
- [10] Brown R.T. and D.C. Smith, *J. App. Phys.* **46**, 402 (1975)
- [11] Fulghum, S.F., and M.M. Tilleman, *J. Opt. Soc. Am. B* **8**, 2401 (1991)
- [12] van Eijk, A.M.J. and L.H. Cohen, "The ANAM-3.0 Development," TNO Physics and Electronics Laboratory, Jun. 2005; Piazzola, J., M.J. van Eijk, G. de Leeuw, *Opt. Eng.* **39**, 1620 (2000).
- [13] Doss-Hammel, S., D. Tsintikidis, D. Merritt and J. Fontana, "Atmospheric Characterization for High Energy Laser Beam Propagation in the maritime Environment," *Proc. SPIE*, vol. 5552, SPIE, Bellingham, WA, 2004, p. 208.
- [14] Bodhaine, B.A., *J. Geophys. Res.* **100**, 8967 (1995); Quinn, P.K., D. J. Coffman, T. S. Bates, E. J. Welton, D. S. Covert, T. L. Miller, J. E. Johnson, S. Maria, L. Russell, R. Arimoto, C. M. Carrico, M. J. Rood, J. Anderson, *J. Geophys. Res.* **109**, D19S01 (2004)

- [15] Sprangle, P., J. R. Penano, A. Ting, B. Hafizi and D.F. Gordon, Journal of Directed Energy 1, **73** (2003)
- [16] Berger P.J., P.B. Ulrich, J.T. Ulrich, and F.G. Gebhardt, Applied Opt. **16**, 345 (1977)
- [17] Gathman, S.G., Opt. Eng. **22**, 057 (1983) ; Gathman, S.G. and K.L. Davidson, "The Navy Oceanic Vertical Aerosol Model," Technical Report 1634, Naval Command, Control and Ocean Surveillance Center, RDT&E Division, San Diego, CA 92152-5001, Dec. 1993.
- [18] Zeisse, C.R., "NAM6: Batch Code fo the Navy Aerosol Model," Technical Report 1804, SPAWAR Systems Center, San Diego, CA 92152-5001, Oct. 1999.
- [19] Berk, A., G.P. Anderson, P.K. Acharya, J.H. Chetwynd, L.S. Bernstein, E.P. Shettle, M.W. Matthew, and S.M. Adler-Golden, "MODTRAN4 User's Manual," Air Force Research Laboratory, Hanscom AFB, MA (2000)
- [20] Gerber, H.E., "Relative Humidity Parameterization of the Navy Aerosol Model (NAM)," NRL Report 8956, pg. 11, Naval Research Laboratory, Washington, DC (1985)
- [21] Shettle, E.P., and R.W. Fenn, "Models for the Aerosols of the Lower Atmosphere and the Effects of Humidity Variations on Their Optical Properties," AFGL-TR-79-0214, Environmental Research Papers No. 676, AFGL, Hanscom AFB, MA (1979).
- [22] Volz, F.E., J. Geophys. Res. **17**, 1017 (1972).
- [23] Volz, F.E., Appl. Opt. **11**, 755 (1972).
- [24] Hale, G.M. and M.R. Querry, Appl. Opt. **12**, 555 (1973)
- [25] Sprangle, P., J.R. Peñano and B. Hafizi, Phys. Rev. E **66**, 046418 (2002)
- [26] Peñano, J.R., P. Sprangle, B. Hafizi, A. Ting, D.F. Gordon, C.A. Kapetanakis, Phys. Plasmas **11**, 2865 (2004)
- [27] "Handbook of Geophysics and the Space Environment," Air Force Geophysical Laboratory, Air Force Systems Command, A.D. Jursa, editor, 1985.
- [28] Spangle, P., J.R. Peñano, B. Hafizi, "*Optimum Wavelength and Power for Efficient Laser Propagation in Various Atmospheric Environments*," NRL/MR/6790-05-8907

- [29] Gebhardt, F.G. and D.C. Smith, IEEE J. Quant. Elec. **7**, 63 (1971); Buser, R.G., R.S. Rohde, P.J. Berger, F.G. Gebhardt, and D.C. Smith, App. Opt. **14**, 2740 (1975).